7. MAGNET ENGINEERING

Leslie Bromberg
Daniel R. Cohn
Richard L. Creedon
Steven P. Grotz
Joel Schultz
Justin Schwartz
Peter Titus
John E. C. Williams

Contents

7. MAGNET ENGINEERING

7.1. INTRODUCTION

The ARIES-I design is a conceptual commercial reactor based on modest extrapolation from the present tokamak physics data base. The ARIES-I reactor operates at a relatively high plasma aspect ratio ($A = 4.5$) and low plasma current ($\sim$11 MA) in order to maximize the bootstrap-current fraction and minimize the amount of plasma current that should be driven by external means. Operation at high aspect ratio and low plasma current in the first magnetohydrodynamic (MHD) stability regime leads to a low value of toroidal beta, which should be compensated for by a high toroidal field. Because the performance of the ARIES-I design is sensitive to the toroidal-field strength, a research effort was undertaken to study the feasibility of high-field toroidal-field (TF) coils utilizing advanced superconductors.

Previous designs have incorporated the use of high fields [1–3]. In this study, the maximum field at the coil of the tokamak is further increased in order to investigate the latest laboratory achievements. Because of the high field and large Lorentz loads, innovative use of high strength materials and support structures is required. The candidate advanced materials for magnets (for the conductor and for the structure) have been limited to those already attained in laboratory tests, although extrapolation to the conductor sizes and lengths required for use in a tokamak power reactor may be needed. Incorporating these concepts and improved materials into toroidal- and poloidal-field (PF) magnets suitable for a commercial tokamak reactor is a difficult challenge. Superconducting materials (both multifilamentary and tape) are discussed in Sec. 7.2. Structural materials such as isotropic steels (316 SS and Incoloy 908) and composite materials are considered and are also discussed in Sec. 7.2.

This research effort resulted in a design for a 24-T (peak field) TF coil using $Nb_3(A\ell,Ge)$ superconductor. Further analysis, however, showed that because $Nb_3(A\ell,Ge)$ is presently only available in the form of tape conductors, losses in the TF coils during the disruption may cause the TF coils to quench. As a result, the reference ARIES-I design uses multifilamentary Nb_3Sn superconductor and achieves a peak field of 21 T at the coil. The stability of high-field superconductors, particularly thick-tape conductors, is discussed in Sec. 7.3. Details of advanced structural designs (*i.e.*, using strong load-carrying stabilizers, grading the conductor, and carefully matching the strains between the different

magnet components) are described in Sec. 7.4. Also discussed are the detailed designs of the reference ARIES-I TF coils, including the finite-element structural analysis, and the 24-T coil utilizing $Nb_3(A\ell,Ge)$ superconductors.

The engineering details of the poloidal-field system for ARIES-I are described in Sec. 7.5. The calculations of the pulse losses in both the TF and PF coils, for both the normal scenario (start-up, burn, and shutdown) and disruptions, are shown in Sec. 7.6. The cost assumptions of the toroidal- and poloidal-field systems are described in Sec. 7.7. Section 7.8 summarizes the results of this ARIES-I magnet-engineering study, including research areas critical to the successful development of high-field magnets for fusion applications, and presents a tentative development plan.

7.2. MATERIALS OPTIONS

7.2.1. Superconductors

The curves in Fig. 7.2-1 represent the boundary between the superconducting and normal regions for zero current density. For a superconducting material to generate a

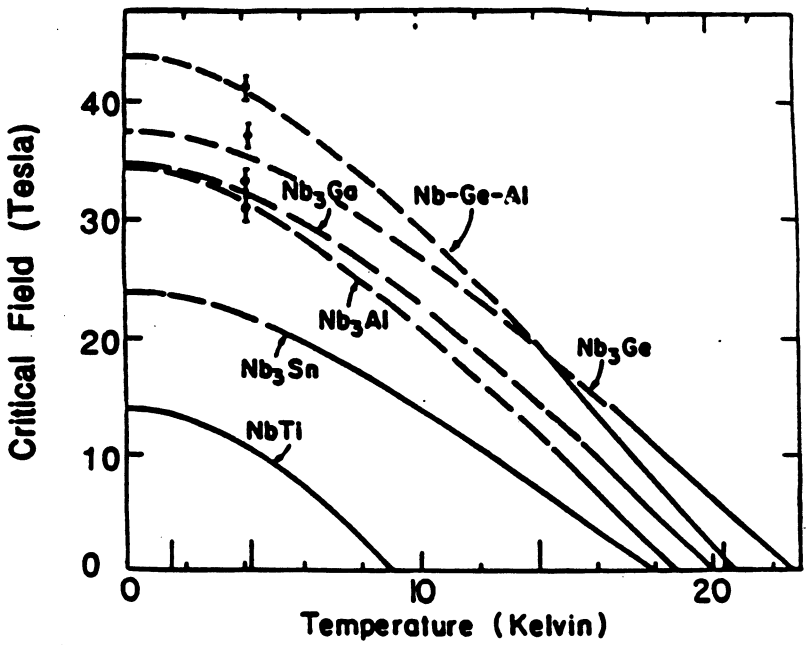

Figure 7.2-1. The upper critical field, $H_{c2}(T)$, for various low-temperature superconducting materials.

magnetic field, the material must have a critical current density, $J_c(B,T)$, of at least 10^8 A/m^2 in the magnetic field. Thus, the operational limits of the materials are below the curves in Fig. 7.2-1. Most superconducting magnets are operated around the boiling point (4.2 K) of liquid helium, therefore the curve of interest for assessing the development of a superconducting material is $J_c(B)$.

The upper critical magnetic field, H_{c2}, as a function of temperature for various low-temperature superconducting materials is shown in Fig. 7.2-1 [4]. Of these materials, only NbTi and Nb_3Sn are available commercially today. Other materials have much higher $H_{c2}(T)$ and thus may be more attractive for high-field coils in the long term. The most promising of these materials are $Nb_3A\ell$ and $Nb_3(A\ell,Ge)$.

NbTi (multifilament). The most common and best understood superconducting material is NbTi. It is easy to produce in multifilamentary cables, and its ductility simplifies magnet fabrication. It has a critical temperature, T_c, of 10 K, and an upper critical field of 14 T. At 4.2 K, it has an operational limit of about 8 T. Although this is not sufficient for the peak field in a high-field toroidal-field (TF) coil, NbTi can be used in the low-field region if the conductor is graded.

Nb_3Sn (multifilament). Other than NbTi, the only commercially available superconductors are Nb_3Sn and its ternary compounds, primarily Nb_3Sn(Ti) and Nb_3Sn(Ta). Numerous techniques exist for producing binary and ternary Nb_3Sn. In general, each technique attempts to provide good mixing between the Nb and the Sn and high-temperature ($\sim$700 °C) heat treatment for growth of the superconducting phase. Critical properties H_{c2}, T_c, and $J_c(B)$ (critical current density) vary with ternary additions and processing. The most widely used method for producing Nb_3Sn is the bronze process, which combines Nb and bronze in a geometry that provides a large contact surface area. The composite is then heat treated ($\sim$700 °C for $\sim$72 h), causing the Sn to diffuse out of the bronze and react with the Nb. At the end of the heat treatment cycle, Nb_3Sn surrounded by impure Cu remains. The best high-field Nb_3Sn-based superconductor, however, has been produced by powder metallurgy processing. In this process, Nb or Nb-1.2 wt % Ti powder is poured into a Cu can containing a central Cu rod. The can is swaged and extruded, and a hole is drilled in the Cu rod. Rods of Sn or Sn-3 wt % Ti are inserted into the drilled hole. The wire is drawn further and heat treated. The critical current density of such powder-metallurgy-produced Nb_3Sn is shown in Fig. 7.2-2 [5].

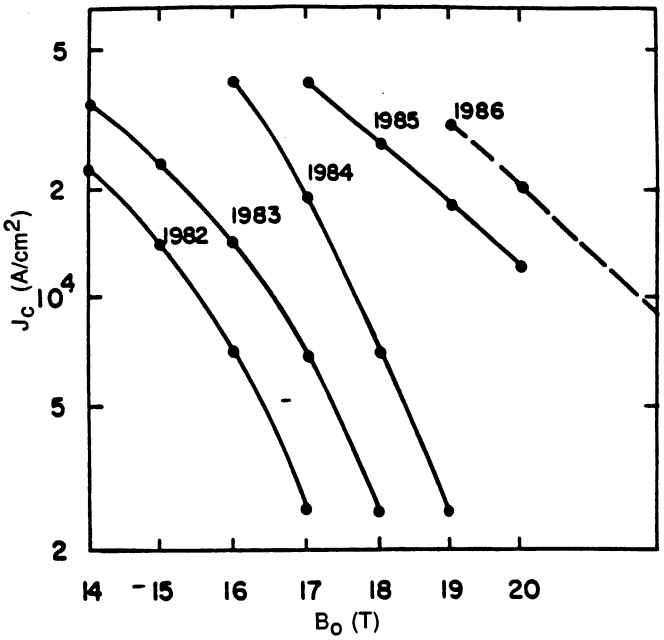

Figure 7.2-2. The critical current density, $J_c(B)$, of powder-metallurgy-produced Nb_3Sn at 4.2 K [5].

$Nb_3A\ell$ and $Nb_3(A\ell,Ge)$ (tape). A family of superconducting intermetallic compounds known as A15, of which Nb_3Sn is a member, are distinguished by their crystal structure and relatively high critical properties, H_{c2} and T_c. The most promising of these compounds, $Nb_3A\ell$ and $Nb_3(A\ell,Ge)$, have critical properties that are significantly better than those of Nb_3Sn (Fig. 7.2-1). Unfortunately, there is no method similar to the bronze or powder metallurgy process for these superconductors and their development has not yet reached the commercial level. Recent progress, however, has led to high current density at high field in small samples. There is no developed method for obtaining high current density (10^8 A/m^2) at high field ($\gtrsim$ 18 T) in the multifilamentary forms of $Nb_3A\ell$ and $Nb_3(A\ell,Ge)$. The best properties have been obtained in superconducting tapes formed by a technique that uses electron and laser-beam heating followed by rapid cooling. The superconductor is formed by passing solid reactants under a high-power beam to heat them, causing the formation of the desired phase. The material then cools rapidly via conduction to a copper substrate and produces the superconductor directly on a copper substrate [6, 7]. This process has produced $Nb_3A\ell$ and $Nb_3(A\ell,Ge)$ conductors with J_c (4.2 K) $\geq 10^8$ A/m^2 in magnetic fields up to 31 T, as shown in Fig. 7.2-3(A) [8]. Although this current density has only been obtained in small samples and no coils have been wound with this material, there is no inherent reason that this process cannot be extrapolated to long lengths of larger conductors.

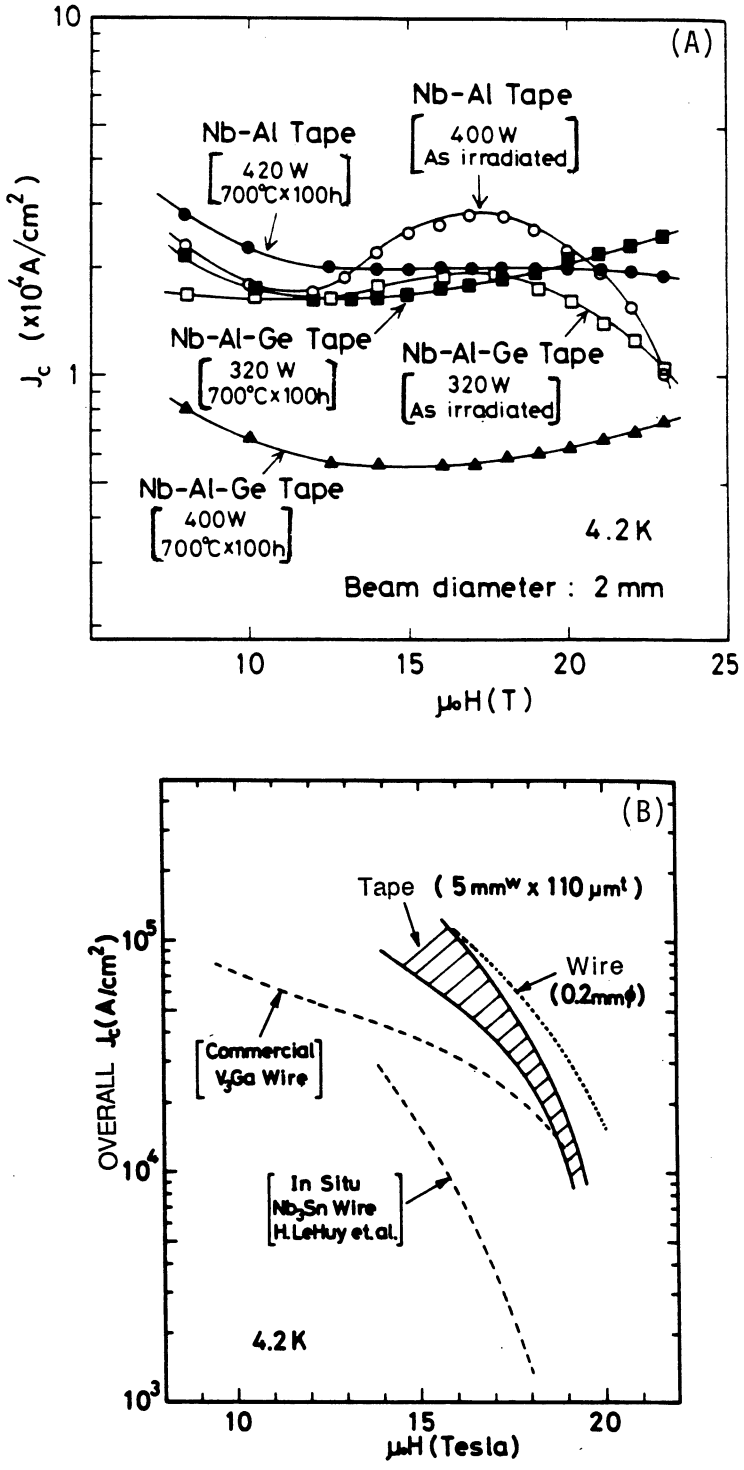

Figure 7.2-3. The critical current density, $J_c(B)$, of (A) $Nb_3A\ell$ and $Nb_3(A\ell,Ge)$ [8] and (B) V_3Ga superconductors.

V_3Ga (multifilament). If superconducting tapes are not sufficiently stable for use in a tokamak and if Nb_3Sn is not sufficiently stable at very high fields, then the alternative superconductor is V_3Ga. As seen in Fig. 7.2-3(B), $J_c(B, 4.2\text{ K})$ for V_3Ga is superior to that for Nb_3Sn. V_3Ga has been used to produce a high-field solenoid and an increase in its use is expected [9, 10].

Strain degradation. For A15 superconducting materials, J_c depends on the mechanical state of the superconductor. As seen in Fig. 7.2-4(A), Nb_3Sn superconductors are very sensitive to mechanical strain, particularly at high field. The strain sensitivities of $Nb_3A\ell$ and V_3Ga are shown in Fig. 7.2-4(B). In general, the strain-induced degradation is related to the reduced magnetic field, $B_r \equiv B/B_{c2}$. Because the developmental A15 materials have higher critical field than Nb_3Sn, larger strains can be tolerated at equal magnetic fields. Furthermore, for equal values of B_r, the developmental A15 materials tend to be more strain tolerant than Nb_3Sn, resulting in significantly better $J_c(\epsilon)$ performance. For $Nb_3A\ell$, this is a result of the relatively small size of $A\ell$ as compared to Sn, which provides more flexibility to the crystal lattice and, thus, a greater ability to withstand deformation. Although resistance to degradation is improved, it may not be sufficient and the effect of mechanical strain on J_c remains a design constraint.

7.2.2. Structural Materials (In-Plane Loads)

Any high-field magnet system experiences very large forces resulting from the Lorentz interaction between the current and the magnetic field. In the TF coil, the structural considerations are particularly important because of the complicated magnetic geometry (toroidal and poloidal fields). In a superconducting TF coil, the loads can be supported by two forms of structure: distributed and bulk. Distributed structure can be either a conduit surrounding the conductor and wound with it, or grooved plates into which the conductor is wound. The stabilizer, present in the conductor for electromagnetic purposes, may also behave as distributed structure. The bulk structure is in the form of a case that defines the outline of the coil. External to the TF coil, a bucking cylinder is required to support the radial loads and a shell-type structure to support the out-of-plane loads. The most important properties for a structural material are strength and modulus. For high magnetic-field applications, an allowable equivalent-tensile strength of about 1200 MPa is sought, with Young's modulus of at least 200 GPa. The thermal expansion from processing temperature to operating temperature is also important because it determines the initial mechanical state of the coil.

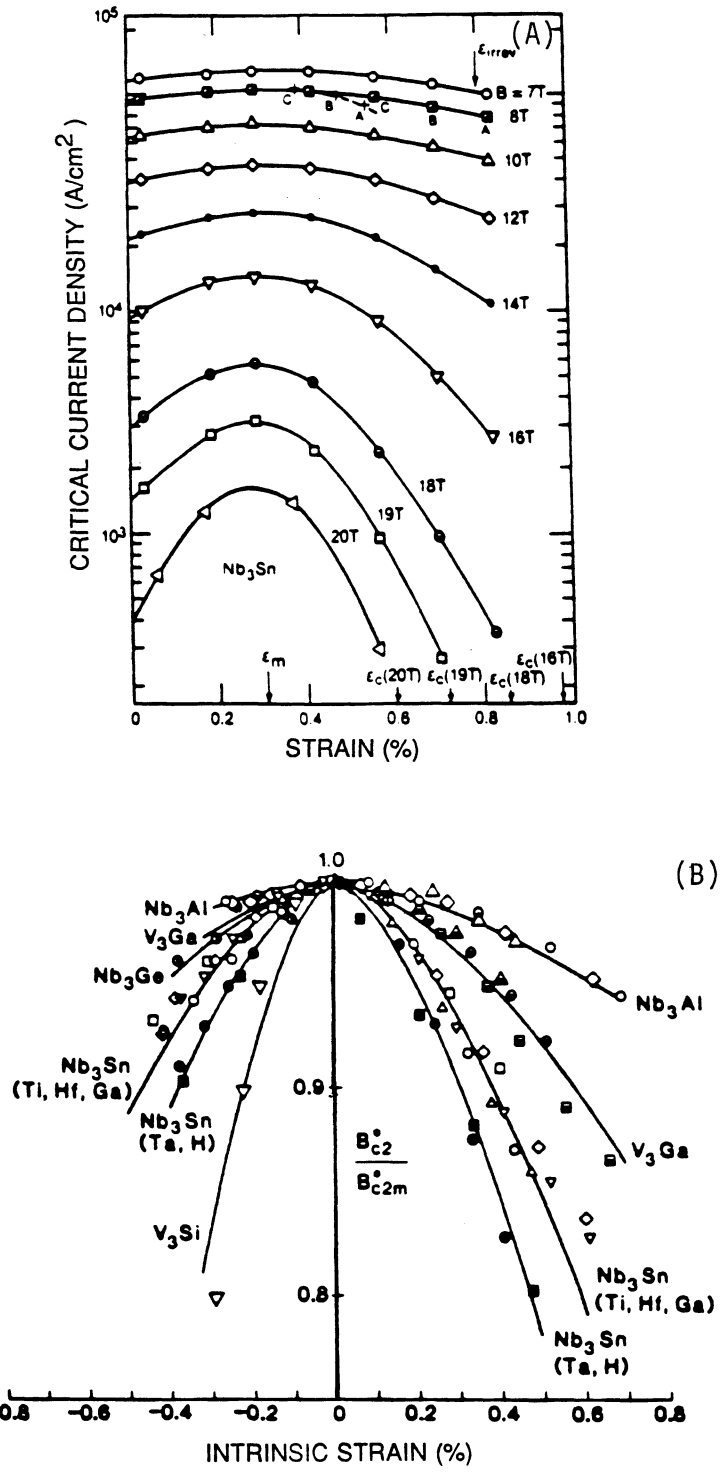

Figure 7.2-4. Strain degradation of the critical current density of (A) Nb_3Sn and (B) A15 superconductors.

The breadth of options for structural materials is illustrated in Fig. 7.2-5. This figure presents structural materials options as functions of availability and experience. The materials can be separated into two categories: isotropic metals and anisotropic fiber composites. Isotropic metals include commercially available steels, superalloys, and titanium alloys. Fibers include polymers (Kevlar), boron, silicon carbide, and carbon. To use a fiber in a component, it must be combined with a matrix material to form a composite. Fibrous composites are inherently anisotropic and require unique design considerations. Materials options have been explored in terms of properties, applicability to a cryogenic system, and level of development. Stabilizer material candidates are discussed separately because they have the additional requirement of high electrical and thermal conductivity.

7.2.2.1. Stabilizer materials

The role of the stabilizer in a superconducting magnet is to provide flux jump stability and quench protection (discussed in detail in Sec. 7.3). The stabilizer must have very high thermal and electrical conductivity. Furthermore, it must be possible to fabricate the conductor so that the stabilizer and superconductor are in intimate contact. Stabilizer options are listed in Table 7.2-I. The rule of mixtures has been used to estimate the

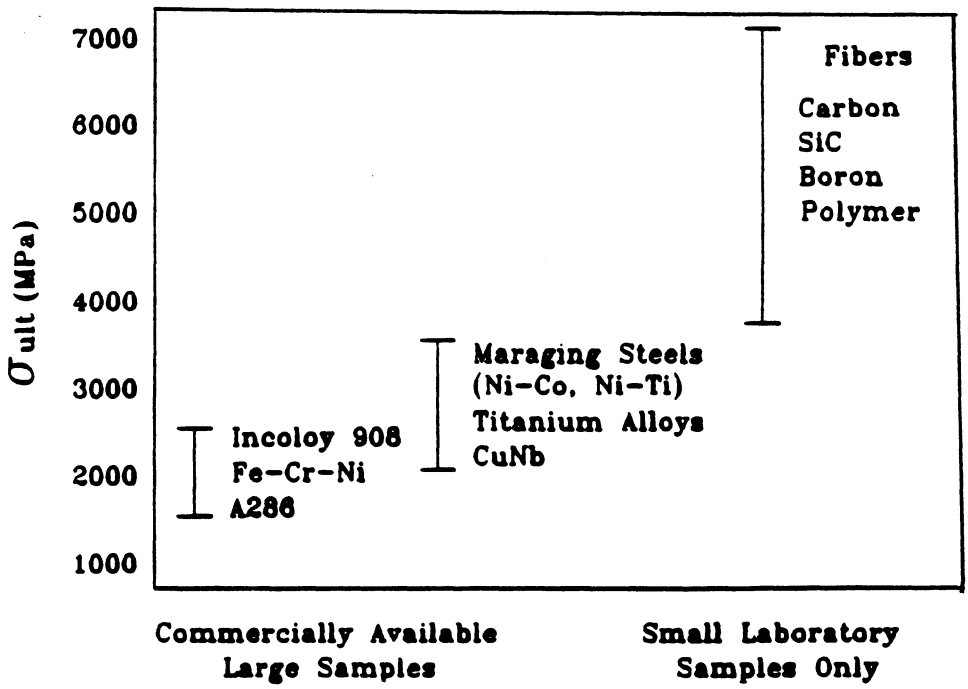

Figure 7.2-5. Structural materials options for high-field superconducting magnets.

Table 7.2-I.
Properties of Advanced Stabilizer Materials

Material	Tensile Strength (MPa)	Tensile Modulus (GPa)	Resistivity[a] (nΩ-m)
Cu	400	120	1.3
Aℓ	200	70	1.3
Aℓ-SiC	1750[b]	217[b]	2[c]
Ti-SiC	1951[b]	213[b]	8[c]
CuNb	2230[b]	142[b]	1.8
CuNb	2850[d]	197[d]	1.8

[a]At 4 K and 24 T.

[b]Properties at 293 K.

[c]Rule of mixtures is used.

[d]Properties at 77 K.

resistivity of the composites. It is not clear that the mechanical properties of Aℓ-SiC in Table 7.2-I were obtained with high purity Aℓ, so either the Aℓ-SiC strength may be decreased or the resistivity increased. The feasibility of combining high strength stabilizer with the superconductor is an important consideration. Obtaining high strength CuNb requires cold working, so Aℓ-SiC may be better suited for applications using cabled superconductors (NbTi, Nb_3Sn), particularly if extended heat treatment is required. Either material may be compatible with $Nb_3Aℓ$ and Nb_3(Aℓ,Ge) tapes.

7.2.2.2. Isotropic metals

High-strength isotropic metals have been considered for the primary structural material. The ultimate tensile stress, $S_{m,t}$, of presently available cryogenic steels is in the range of 1.6–2.0 GPa (304 SS, 316 SS, JBK–75, Incoloy 908, and Fe-Mn and Fe-Cr alloys), leading to an allowable equivalent stress in the neighborhood of 600–1000 MPa. The best materials are the Fe-Cr-Ni and Fe-Mn-Cr alloys developed in Japan specifically for cryogenic applications [11, 12] and cold-worked-then-aged Incoloy 908 [13–15].

The Fe-Cr-Ni and Fe-Mn-Cr alloys are distinguished by high strength and fracture toughness at liquid helium temperature. Figure 7.2-6 shows the trade-off between strength and toughness for commercially prepared Fe-Cr-Ni and Fe-Mn-Cr, in addition to traditional cryogenic steels (NIST trend line), and Incoloy 908. The JAERI Box refers to properties targeted by the Japanese ($\sigma_y \geq 1200$ MPa with $K_{Ic} \geq 200$ MPa-m$^{1/2}$) that provide the high strength and crack-growth resistance required for a PF coil. This goal has been achieved with the Fe-Cr-Ni system. For a TF coil operating in a steady-state tokamak, it is preferable to have an alloy at the high strength end of the σ_y *versus* K_{Ic} curve. Further alloying of Fe-Cr-Ni may obtain higher strength at reduced toughness.

The best combination of strength and toughness is obtained with Incoloy 908. This alloy was recently developed at the Massachusetts Institute of Technology and is distinguished by a very low coefficient of thermal expansion (matched to that of Nb_3Sn), which reduces the thermal strain in the superconductor. It is very ductile at 4 K (strain-to-failure rate is $> 20\%$) and is both workable and weldable. It requires a heat treatment schedule that is similar to that required for Nb_3Sn, so Incoloy 908 is an ideal magnet material. Development of this material continues, and $\sigma_y \sim 1800$ MPa with $K_{Ic} > 200$ MPa-m$^{1/2}$ is anticipated [15].

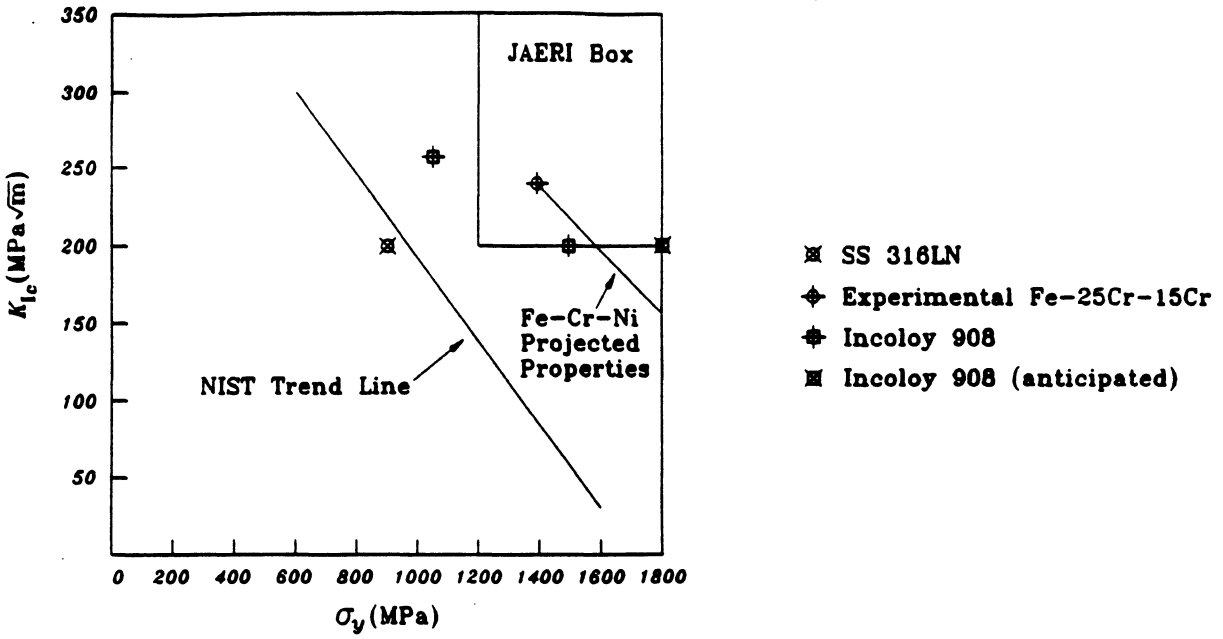

Figure 7.2-6. The toughness, K_{Ic}, as a function of strength, σ_y, for cryogenic steels.

7.2.2.3. Composites

Composite materials may be capable of simultaneously obtaining higher strength, stiffness, and fracture toughness than metals. Fiber-matrix compatibility during all stages of fabrication and operation is a critical issue in materials selection. Thus, the selection of fiber and matrix are inherently interdependent. Although prediction of behavior is complicated by the anisotropy of fibrous composites, it may be possible to tailor the mechanical properties to a specific loading. Consideration must be given not only to the properties of the constituent materials, but also to the ability to fabricate the composite with satisfactory properties in every direction and at the fiber/matrix interface. Because of the multidimensionality of the stress state (vertical tension, radial compression, and shear) in the inner leg of a TF coil, high strength is required in more than one direction. Fiber and matrix options have been assessed and the most promising material system has been selected. A method of predicting the resulting composite behavior has been developed in terms of: (1) mechanical properties, (2) load distribution between fiber and matrix, and (3) fatigue strength. A design criterion based upon the anisotropic behavior has also been developed.

Traditionally, composites use an epoxy or aluminum matrix. These composites have very good strength-to-weight ratio, the figure of merit for aerospace applications. For a superconducting TF magnet, however, the important parameters are the vertical tensile strength and modulus and the radial compressive strength. Because fibers tend to have relatively low compressive strength, it is necessary to incorporate the fibers into a matrix that is capable of supporting the compressive loads in the inner leg. To obtain high strength in all directions, only metal-matrix composites are considered. The leading candidates for the matrix material are the isotropic metals (Incoloy 908 and Fe-Cr-Ni). Figure 7.2-7 illustrates the strength/stiffness trade-off for the various fiber options. Of these, the best combination of mechanical properties, availability, cost, and applicability is found in carbon. Carbon fibers have been reported with the longitudinal tensile strength, $S_{f11,T} \gtrsim 7$ GPa, and with the longitudinal Young's modulus, $E_{f11} \sim 900$ GPa (not simultaneously) [16–18]. The fibers are inherently anisotropic, with the transverse Young's modulus, $E_{f22} < 0.1\ E_{f11}$, that may prove advantageous for TF-coil structural applications. By aligning the fibers with the vertical (tensile) load, the fibers provide very high vertical modulus and strength. Because of the very low E_{f22}, however, the radial load is concentrated in the matrix. Thus, the loads are concentrated in the material best suited to support them.

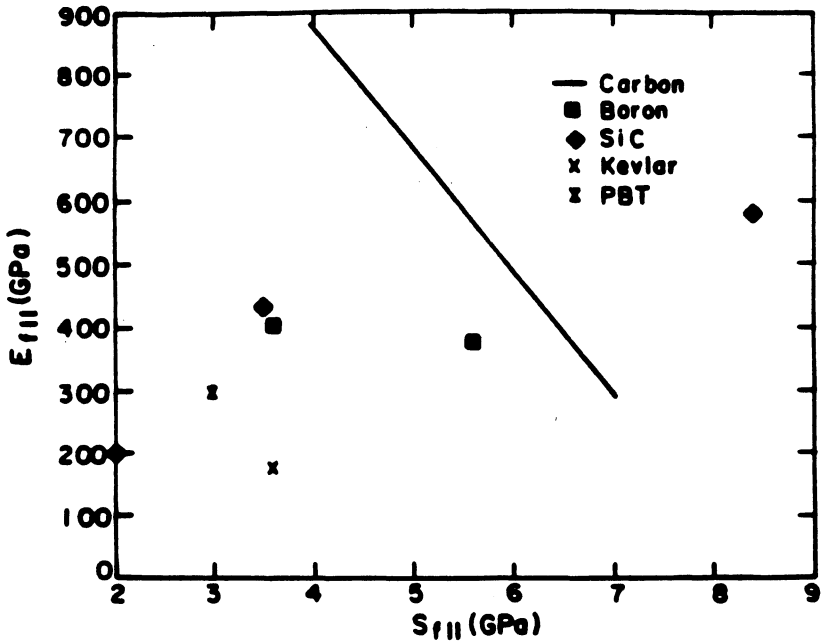

Figure 7.2-7. Longitudinal Young's modulus, E_{f11}, as a function of longitudinal tensile strength, $S_{f11,T}$, for various fibers.

Carbon fibers retain very good mechanical properties over a broad temperature range. For application in a metal-matrix composite, however, one serious limitation must be overcome: high temperature interactions with nickel. Because Ni is a key ingredient in high-strength cryogenic steels, these interactions are particularly important for a superconducting-magnet structural material. Recent results from American Cyanamid and NIST indicate that C/Ni interactions can be prevented by coating carbon fibers with a thin Co/W diffusion barrier that stabilizes the interface [19].

7.2.2.4. Prediction of composite properties

Composite mechanical properties have been predicted by applying the approach of linear composite theories originally developed for epoxy-matrix composites. At low temperature, experience from epoxy-matrix materials is applicable because all of the matrix materials under consideration are in the linear regime of behavior. Load sharing between fibers and matrix, as well as the effect of voids, has been considered. Furthermore, a failure criterion based upon the properties has been developed and the improvement of effective fracture toughness (decrease in stress concentration factor) due to the presence of fibers also has been estimated. Only orthotropic composites have been considered.

Table 7.2-II provides a list of the bulk composite properties that were calculated from fiber and matrix properties. Fibers are uniaxial in the '1' direction. The required fiber and matrix properties are listed in Tables 7.2-III and 7.2-IV, and the correlation factors of theory and experiment are listed in Table 7.2-V. The composite properties of Table 7.2-II have been calculated in terms of the parameters in Tables 7.2-III, 7.2-IV, and 7.2-V, and in terms of the fiber, matrix, and void volume fractions, respectively, k_f, k_m, k_v.

The composite strength is anisotropic and varies between tension and compression. The tensile strength in the fiber direction, $S_{c11,T}$, has been calculated based upon rule of mixtures:

$$\begin{aligned} S_{c11,T} &= k_{f,eff}\, S_{f11,T} + k_{m,eff}\, S_{matrix}\,, \\ k_{f,eff} &= k_f(1-k_v)\,, \\ k_{m,eff} &= k_m(1-k_v)\,, \end{aligned} \tag{7.2-1}$$

Table 7.2-II.
Calculated Bulk Composite Properties

Tensile strength parallel to fibers	$S_{c11,T}$
Compressive strength parallel to fibers	$S_{c11,C}$
Tensile strength normal to fibers	$S_{c22,T}$
Compressive strength normal to fibers	$S_{c22,C}$
Shear strength	$S_{c12,S}$
Young's modulus parallel to fibers	E_{c11}
Young's modulus normal to fibers	E_{c22}
Shear modulus in plane of fibers	G_{c12}
Shear modulus in plane normal to fibers	G_{c23}
Poisson's ratio in plane of fibers	ν_{c12}
Poisson's ratio in plane normal to fibers	ν_{c23}
Anisotropy correlation factor	K_{c12}
Minimum fiber volume fraction	$k_{f,min}$

Table 7.2-III.
Required Fiber Properties

Longitudinal tensile strength	$S_{f11,T}$
Limiting tensile strain	$\epsilon_{fl,T}$
Longitudinal Young's modulus	E_{f11}
Transverse Young's modulus	E_{f22}
Shear modulus in fiber plane	G_{f12}
Shear modulus normal to fibers	G_{f23}
Poisson's ratio in fiber plane	ν_{f12}
Poisson's ratio normal to fibers	ν_{f23}

Table 7.2-IV.
Required Matrix Properties

Tensile strength (isotropic)	$S_{m,T}$
Compressive strength (isotropic)	$S_{m,C}$
Yield stress	$\sigma_{m,y}$
Limiting tensile strain	$\epsilon_{ml,T}$
Limiting compressive strain	$\epsilon_{ml,C}$
Limiting shear strain	$\epsilon_{ml,S}$
Young's modulus (isotropic)	E_m
Shear modulus (isotropic)	G_m
Poisson's ratio (isotropic)	ν_m

Table 7.2-V.
Theory–Experiment Correlation Factors

Fiber tension	β_{fT}
Matrix tension	β_{mT}
Fiber compression	β_{fC}
Matrix compression	β_{mC}
Composite normal to fibers, tension	β_{22T}
Composite, normal to fibers, compression	β_{22C}
Composite, fiber plane, shear	β_{12S}
Load coupling factor	$K_{c12\alpha\beta}$

where S_{matrix} represents the load carrying ability of the matrix in the presence of the fiber and $k_{f,eff}$ and $k_{m,eff}$ are, respectively, the effective fiber and matrix fractions. Because of the high strength and stiffness of the fibers, the matrix will not support load beyond yield. However, if the fiber fracture strain, $\epsilon_{fl,T}$, is reached before matrix yielding occurs, then the matrix stress is governed by the fiber fracture strain. Thus,

$$S_{matrix} = MIN\{\sigma_{m,y},\, E_m\, \epsilon_{fl,T}\}\,, \tag{7.2-2}$$

where MIN indicates that the minimum of the bracketed terms is used. For epoxy-matrix composites, $S_{matrix} \ll S_{f11,T}$. Requiring that the composite is stronger than the unreinforced matrix ($S_{c11,T} \geq S_{m,T}$), one obtains the minimum fiber-volume fraction

$$k_{f,min} = \frac{S_{m,T} - S_{matrix}}{S_{f11,T} - S_{matrix}}\,. \tag{7.2-3}$$

The other composite strengths have been predicted in a similar manner.

Because of the inherent anisotropy of composite materials, the ASME design criterion relating the strength of a material to an allowed-equivalent tensile stress is not applicable. A design criterion based upon composite mechanical properties in all directions and dependent upon the geometry of the loading relative to the composite has been developed.

For a 3-D loading, Hoffman proposed that fracture occurs when [20]

$$A(\sigma_y - \sigma_z)^2 + B(\sigma_z - \sigma_x)^2 + C(\sigma_x - \sigma_y)^2 + 2L\tau_{yz}^2 + 2M\tau_{zx}^2 + 2N\tau_{xy}^2 \geq 1 , \quad (7.2\text{-}4)$$

where A, B, C, L, M, and N are related to the composite strengths in the various directions, and σ_x, σ_y, σ_z, τ_{yz}, τ_{zx}, and τ_{xy} are the applied stresses. The design criterion then limits the left–hand side of Eq. (7.2-4) to an appropriate fraction of unity. For a 2-D loading, a fracture condition can be written as [21]

$$\begin{cases} F < 0, & \text{fracture occurs} \\ F = 0, & \text{onset of fracture} \\ F > 0, & \text{no fracture} \end{cases} , \quad (7.2\text{-}5)$$

where

$$F \equiv 1 - \left[\left(\frac{\sigma_{c11,\alpha}}{S_{c11,\alpha}} \right)^2 + \left(\frac{\sigma_{c22,\beta}}{S_{c22,\beta}} \right)^2 + \left(\frac{\sigma_{c12,S}}{S_{c12,S}} \right)^2 - K_{c12\alpha\beta} K_{c12} \frac{\sigma_{c11,\alpha}\, \sigma_{c22,\beta}}{|S_{c11,\alpha}|\, |S_{c22,\beta}|} \right] , \quad (7.2\text{-}6)$$

S_c and σ_c refer to, respectively, the composite strength and applied stress in the indicated direction ('1' direction is parallel to the fibers), and α and β refer to, respectively, tension and/or compression. A load coupling factor, $K_{c12\alpha\beta}$, accounts for the differences between tension-tension (TT), tension-compression (TC), compression-tension (CT), and compression-compression (CC). The anisotropy correlation factor, K_{c12}, accounts for the effects associated with the anisotropy in the composite Young's modulus and Poisson's ratio (derived by Chamis [22]). For an isotropic material, Eq. (7.2-6) reduces to the von Mises distortion energy criterion. The determination of $K_{c12\alpha\beta}$ is based on composite experience. As expected, mixed modes (TC and CT) fracture at lower stress levels than hydrostatic modes (TT and CC). By defining a new fracture parameter, G, one can write

$$G \equiv 1 - F , \quad (7.2\text{-}7)$$

and the fracture condition becomes

$$\begin{cases} G > 1, & \text{fracture occurs} \\ G = 1, & \text{onset of fracture} \\ G < 1, & \text{no fracture} \end{cases} . \quad (7.2\text{-}8)$$

A design criterion of $G < 1/3$ is consistent with the ASME criterion of 1/3 of ultimate tensile stress. Note that G depends on both the material properties and the specifics of the stress state, so the composite design must be coupled to the magnet design.

7.3. FLUX JUMP STABILITY

At present, the superconducting materials for very high magnetic fields (> 21 T), $Nb_3A\ell$ and $Nb_3(A\ell,Ge)$, are only available in the form of tape. Although tape superconductors may simplify conductor fabrication by eliminating cabling, they are inherently unstable to magnetic flux jumps and their use will lead to additional design constraints [23]. A detailed analysis of the flux jump stability of tape superconductors has been conducted and provides a stability criterion based upon magnetothermal characteristics.

The general equations governing flux jump are Maxwell's equations

$$\nabla \times E = -\frac{\partial B}{\partial t}, \tag{7.3-1}$$

$$\nabla \times B = \mu_o J, \tag{7.3-2}$$

and the heat-conduction equation

$$C\frac{\partial T}{\partial t} = \nabla \cdot \kappa \nabla T + E \cdot J. \tag{7.3-3}$$

These equations have been solved using linear perturbation theory and a 2-D variational approach. Because the fully 2-D, edge-cooled stabilized tape is very complicated mathematically, two simplified geometries (representing the worst and best cases) were examined first. The simplified cases provide an upper and lower bound to the stable parameter space and useful insight into the physics of the complete problem. The full problem was then solved and an analytic stability criterion determined. These results were compared to the 1-D calculation performed by Hart [23].

A lower bound to the conductor stability is found by analyzing a 1-D, unstabilized tape superconductor. The external magnetic field was assumed normal to the tape and the critical state model for magnetic field penetration into a Type II superconductor was applied [24]. The resulting stability criterion is

$$\mu_o^2 J_c^2 p^2 = B_o^2 < \mu_o C_{sc} (T_c - T_o) \left(\frac{\pi}{2}\right)^2, \tag{7.3-4}$$

where J_c is the superconductor critical current density, p is the penetration depth of the magnetic field into the superconductor, B_o is the external magnetic field, C_{sc} is the specific heat of the superconductor, and T_c and T_o are, respectively, the critical and operating temperatures.

An upper bound to the stability is obtained by considering a 2-D tape in contact with a perfectly conducting stabilizer ($\kappa_{st} \rightarrow \infty$, $\rho_n \rightarrow 0$). For these conditions, the stability criterion is

$$\mu_o J_c^2 \frac{d_{sc}^2 p^2}{d_{sc}^2 + p^2} < \frac{C_{sc} T_c^2}{T_c - T_o} \left(\frac{\pi}{2}\right)^2 , \tag{7.3-5}$$

where d_{sc} is the thickness of the superconductor.

Lastly, the tape was analyzed using finite thermal properties in both the conductor and the stabilizer. Variational principles describing the system were written and integrated using 2-D temperature and flux profiles. The resulting dispersion relation for the linear growth rate was analyzed to locate the marginal stability condition. The resulting stability criterion is

$$p^2 J_o^2 \leq \frac{16}{5} \frac{T_c - T_o}{\rho_n} \frac{f_{st}^3}{f_{sc}^2} \kappa_{st} \left(1 + \frac{4}{5} \frac{f_{st}}{f_{sc}} \frac{\kappa_{st}}{\kappa_{sc}} \frac{d_{sc}^2}{p^2}\right)^{-1} , \tag{7.3-6}$$

where ρ_n is the stabilizer resistivity, κ_{sc} and κ_{st} are, respectively, the superconductor and stabilizer thermal conductivities, and f_{sc} and f_{st} are, respectively, the fractions of superconductor and stabilizer in the conductor ($f_{sc} + f_{st} = 1$). A comparison of these results to Hart's stability criterion is shown in Fig. 7.3-1 for $p = w = 0.01$ m, where w is the half width of the tape. In general, the 2-D effects reduce the stability of the tape relative to Hart's 1-D analysis. These 2-D effects become dominant as $d_{sc} \rightarrow 0.1w$,

7.4. TOROIDAL-FIELD COIL DESIGNS

One of the primary goals of the ARIES study is to identify key areas of physics and technology that may lead to attractive tokamak reactors. Because the performance of the ARIES-I design is sensitive to the toroidal-field strength, a research effort was undertaken to study the feasibility of high-field toroidal-field (TF) coils that utilize advanced superconductors which are available, at least, as laboratory samples. This effort resulted in the design of a 24-T (peak field) TF coil using $Nb_3(A\ell,Ge)$ superconductor. Further analysis, however, showed that because $Nb_3(A\ell,Ge)$ is presently only available in the form of tape conductors, losses in the TF coils during the disruption may cause the TF coils to quench. As a result, the reference ARIES-I design uses multifilamentary Nb_3Sn superconductor and achieves a peak field of 21 T at the coil. In this section, the TF-coil constraints and concepts are reviewed. The detailed design of the reference ARIES-I TF coils, including the structural analysis is also given. Finally, the design of the 24-T coil that utilizes $Nb_3(A\ell,Ge)$ superconductors is discussed.

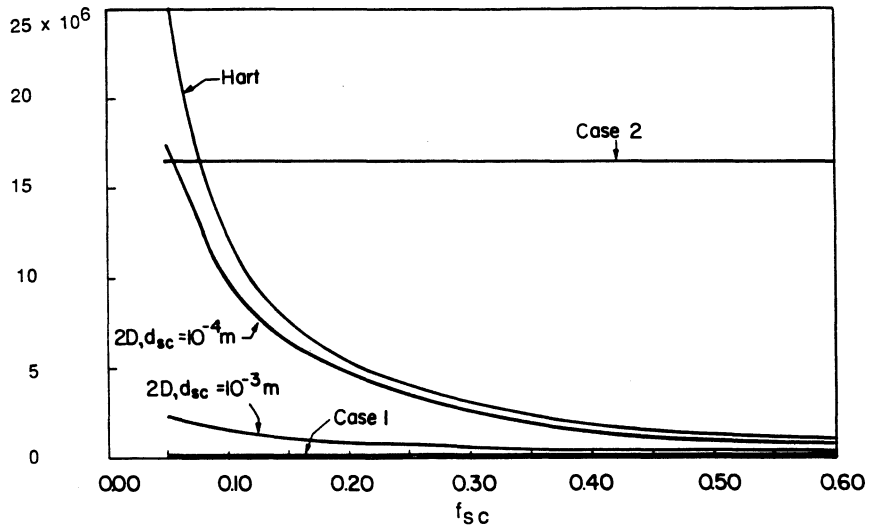

Figure 7.3-1. Stability conditions for simple cases 1 and 2, the full 2-D condition, and Hart's condition ($w = 0.01$ m).

7.4.1. Constraints

Although the development of a superconducting magnet depends upon obtaining a superconductor capable of carrying sufficient current density at the desired field, this is only one of many considerations. The ARIES-I design minimizes the size of the TF-magnet system subject to the following restrictions:

- Superconductor critical current,
- Superconductor stability,
- Quench protection,
- Superconductor strain,
- Stress and strain in structural materials,
- Heat removal,
- Pumping power,
- Conductor fabrication,
- Magnet construction.

7.4.2. Concepts

A conceptual design for the 21-T magnet has been developed based upon isotropic structural materials. Furthermore, two conceptual designs for the 24-T TF magnet have been developed: one based upon isotropic structural materials and one utilizing composite materials. All three design concepts use structural plates formed with grooves into which the conductor is wound. Thus, rather than winding all of the materials in the magnet, only the conductor requires winding. This facilitates fabrication by removing the stiffest material from the winding process. The cross section of the ARIES-I TF coil, shown in Fig 7.4-1(A), illustrates the plate design. A schematic diagram of a typical turn, showing the main parameters is illustrated in Fig 7.4-1(B).

Because of its superior mechanical properties and low coefficient of thermal expansion, Incoloy 908 has been selected as the base material for the plates. For the coil cases, Fe-Cr-Ni is preferred so that the differential thermal contraction will induce a compressive pre-strain in the conductor and in the plates. An equivalent tensile stress of 1000 MPa has been allowed for the isotropic design. Based upon the proposed design criterion for cryogenic systems [25], steel is required to have $\sigma_y \geq 1500$ MPa and $S_{m,T} \geq 2000$ MPa at 4 K. For the composite material, the 2-D orthotropic design criterion (Sec. 7.2.2.4) is applied. For the stabilizer material, an allowable stress of 800 MPa and Young's modulus of 185 GPa are used. Because of its superior strength and isotropic properties, CuNb is preferable to Aℓ-SiC as the stabilizer.

In a high-field magnet, the stored energy is sufficiently large that stabilizer requirements are dictated by quench protection and not by stability. In the ARIES-I magnet, the allowed stabilizer current density is increased by two mechanisms: (1) increasing the winding pack current, I_{pack}, which becomes feasible in the plate geometry and (2) halving the effective stored-energy per coil, E_{stored}, by adding an extra layer of electrical insulation between the center plates in each coil. Each half coil is then driven by a separate power supply and current lead. Thus, although there are 16 coils mechanically, there are 32 coils electromagnetically.

Although optimizing every turn of the conductor separately results in the absolute minimum size of the magnet, it also leads to an excessive number of joints (= no. of coils $\times$ no. of rows). Using the same conductor everywhere, however, is very inefficient. As a compromise, the ARIES-I coil uses five conductor grades. Because the depths of the grooves in the plates are determined by the design of the conductor, a different depth is required for each grade.

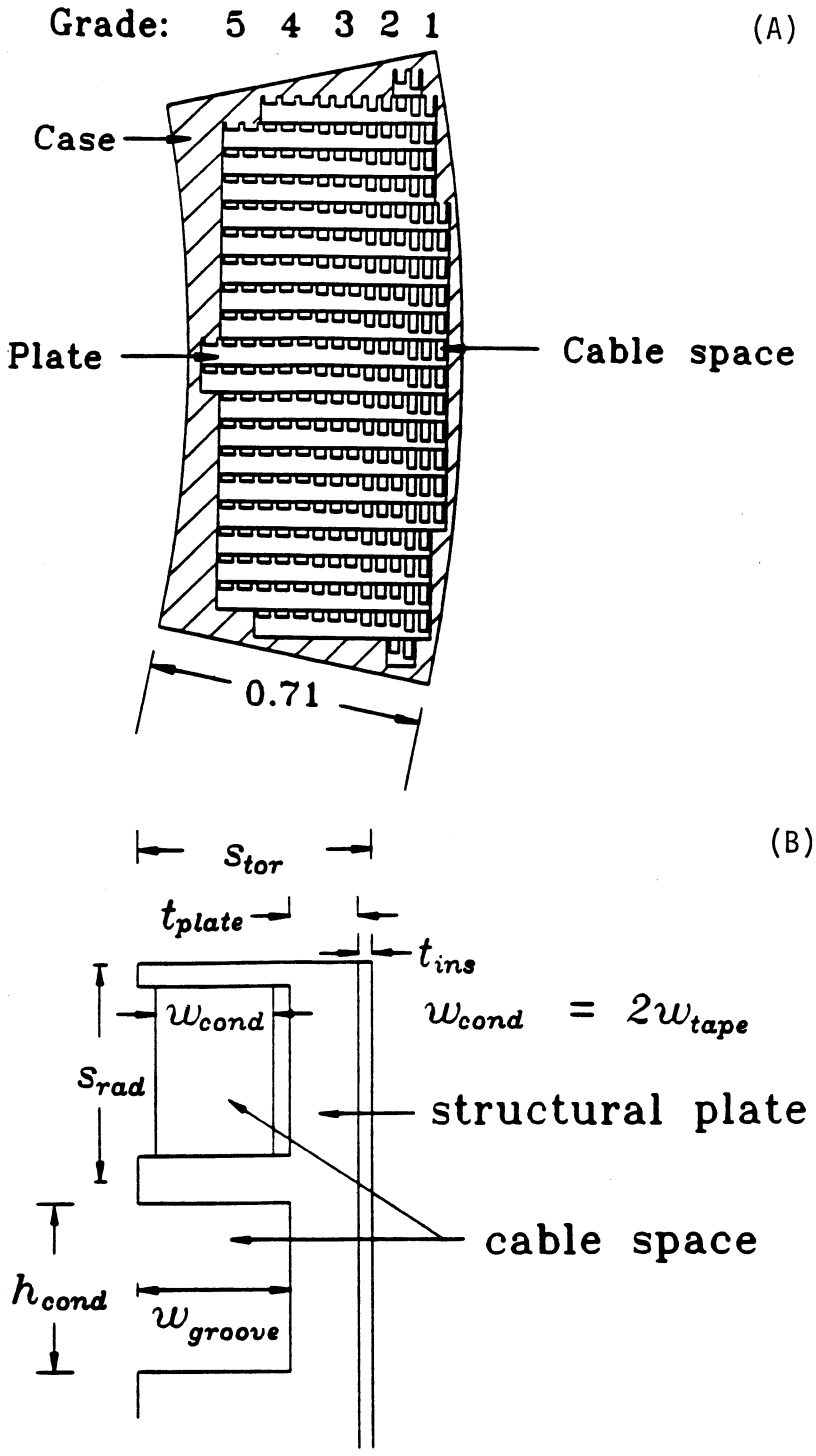

Figure 7.4-1. (A) The cross section of the inner leg of the reference ARIES-I TF-coil design, illustrating the structural plate concept; and (B) Schematic diagram of a typical turn, indicating the main design parameters.

7.4.3. The ARIES-I Reference Toroidal-Field Coil Design

The reference ARIES-I TF coil has a peak field of 21 T and is based upon more conservative materials-development assumptions than the 24-T coil. For this design, all of the superconductor is multifilamentary (NbTi, Nb_3Sn, and V_3Ga if necessary) and all of the structural material is isotropic steel (either 316 SS or Incoloy 908). Coil design parameters are given in Table 7.4-I, conductor grading information is in Table 7.4-II, and design results are shown in Table 7.4-III.

Table 7.4-I.
TF-Coil Design Parameters for the ARIES-I Reactor

Magnetic field (T)	21.04
I_{pack} (kA)	100
V_{max} (kV)	20
S_{max} (A^2-s/m^4)	5×10^{16}
Number of coils	16
Ripple on axis	0.15%
Ripple on edge	1.49%
Thermal contraction (from 293 to 4 K)	
Superconductor	2×10^{-3}
Stabilizer	3×10^{-3}
Plate	2×10^{-3}
Case	3×10^{-3}
Insulation	2×10^{-3}

Table 7.4-II.
Conductor-Grading Design Parameters for the ARIES-I Reactor

Grade	1	2	3	4	5
Maximum field (T)	21.1	18.	14.	9.	4.
J_c (10^8A/m^2)	2.40	4.98	12.5	35.5	46.5
T_c (K)	4.6	6.5	9.1	12.4	6.6
s_{tor} (cm)	7.0	7.0	7.0	7.0	7.0
s_{rad} (cm)	3.8	4.0	4.4	5.0	5.1
t_{plate} (cm)	1.85	3.28	4.30	4.84	4.96
h_{cond} (cm)	2.10	2.30	2.70	3.30	3.41
$w_{cond} = w_{groove}$ (cm)	4.95	3.55	2.56	1.90	1.84
t_{ins} (cm)	0.2	0.2	0.2	0.2	0.2
f_{sc}	0.433	0.269	0.128	0.032	0.038
f_{st}	0.567	0.731	0.872	0.968	0.962

7.4.3.1. Structural Analysis

Support of the electromagnetic forces acting on the TF coils is provided by three structural members: two torque shells and a bucking cylinder (Fig. 7.4-2). The torque shells are axisymmetric toroidal caps that counteract the overturning forces in the upper and lower hemispheres. The arrangement of loads is such that comparatively small forces have to cross the machine mid-plane, most being balanced in their own hemisphere. The small overturning forces at the outboard mid-plane are constrained by stiffness of the leg of the TF coil. The bucking cylinder restrains the inward radial forces of the TF coil, as well as a small overturning force on the inner leg of the coil. There is zero torque on the components where the top and bottom of the bucking cylinder meet the torque shells. There is little or no force transmitted between the cylinder and the shells and, therefore, very little interconnecting structure is required.

Table 7.4-III.
TF-Coil Design Results for the ARIES-I Reactor

Radial build (m)	0.71
J_{magnet} (MA/m^2)	25.7
J_{st} (MA/m^2)	156
E_{stored} (total, GJ)	132
E_{stored} (circuit, GJ)	4.1
Vertical stress, stabilizer (MPa)	774
Vertical stress, case (MPa)	888
Area fraction (%)	
Superconductor	3.9
Stabilizer	14.0
Plate	54.8
Case	19.9
Helium	1.6
Insulation	6.1

The ANSYS computer code has been used to analyze a model of the ARIES-I reactor for in-plane and out-of-plane loads. The model is cyclically symmetric and consists of a wedge that is 1/16 of the machine. It is also symmetric about the equatorial plane. The 3-D model was created from a 2-D axisymmetric model by rectilinear expansion of the TF coil to a two solid-element thickness, and cylindrical expansion of the shell to a four solid-element thickness. The TF coil and shell nodes are fully aligned only at the vertical mid-plane of the wedge.

Figure 7.4-3 shows the finite-element models of the ARIES-I TF coil and support structure. The TF coil is bucked against a bucking cylinder. Gaps between the TF coils ensure that the coils do not wedge against each other. The cross section of the coil is kept constant. For modeling purposes, coupling has been introduced between the coil and the bucking cylinder to allow transmission of radial loads but at the same time preventing the transmission of vertical loads from the TF coil to the bucking cylinder; these gaps

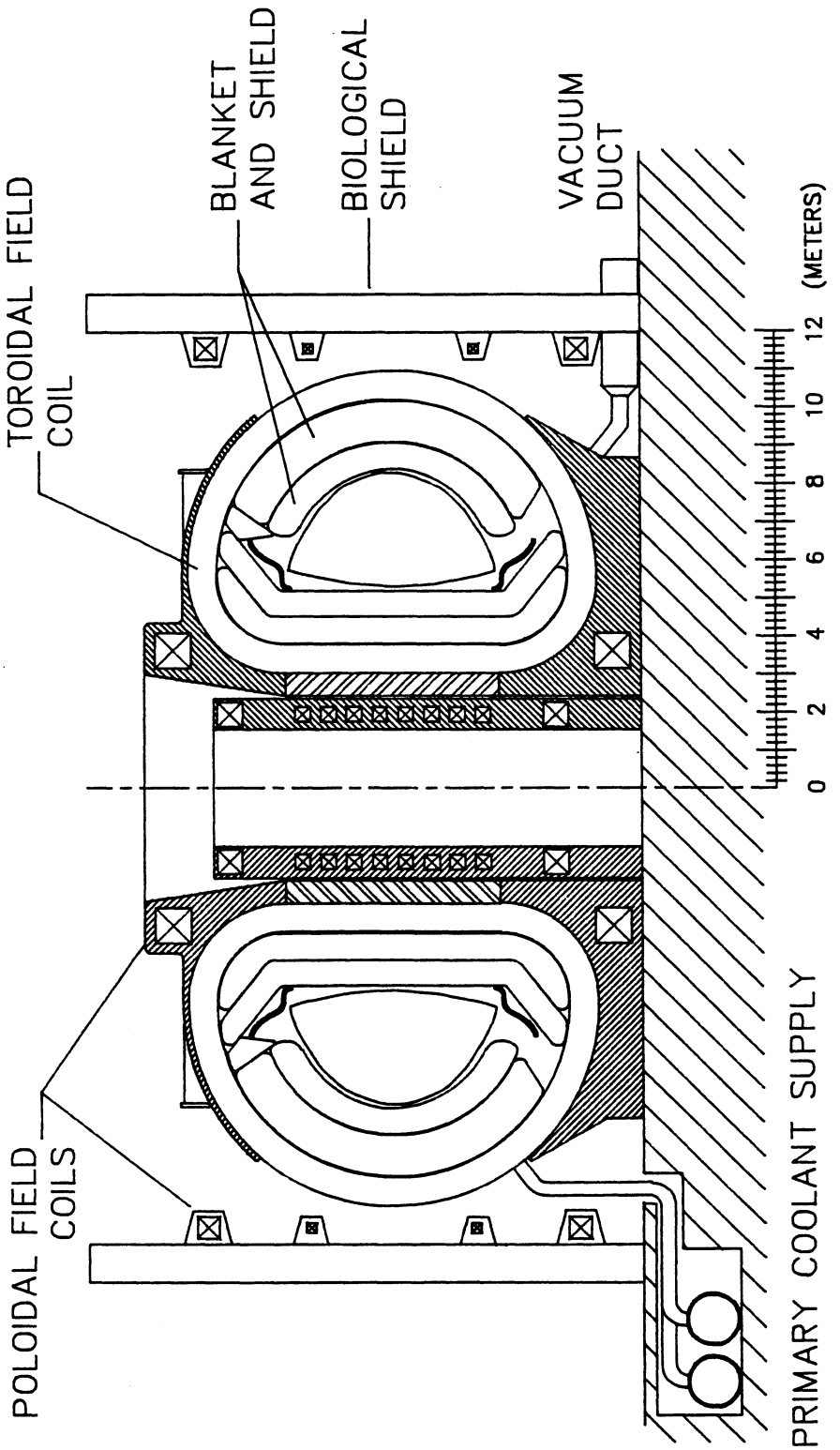

Figure 7.4-2. Elevation view of the ARIES-I fusion power core.

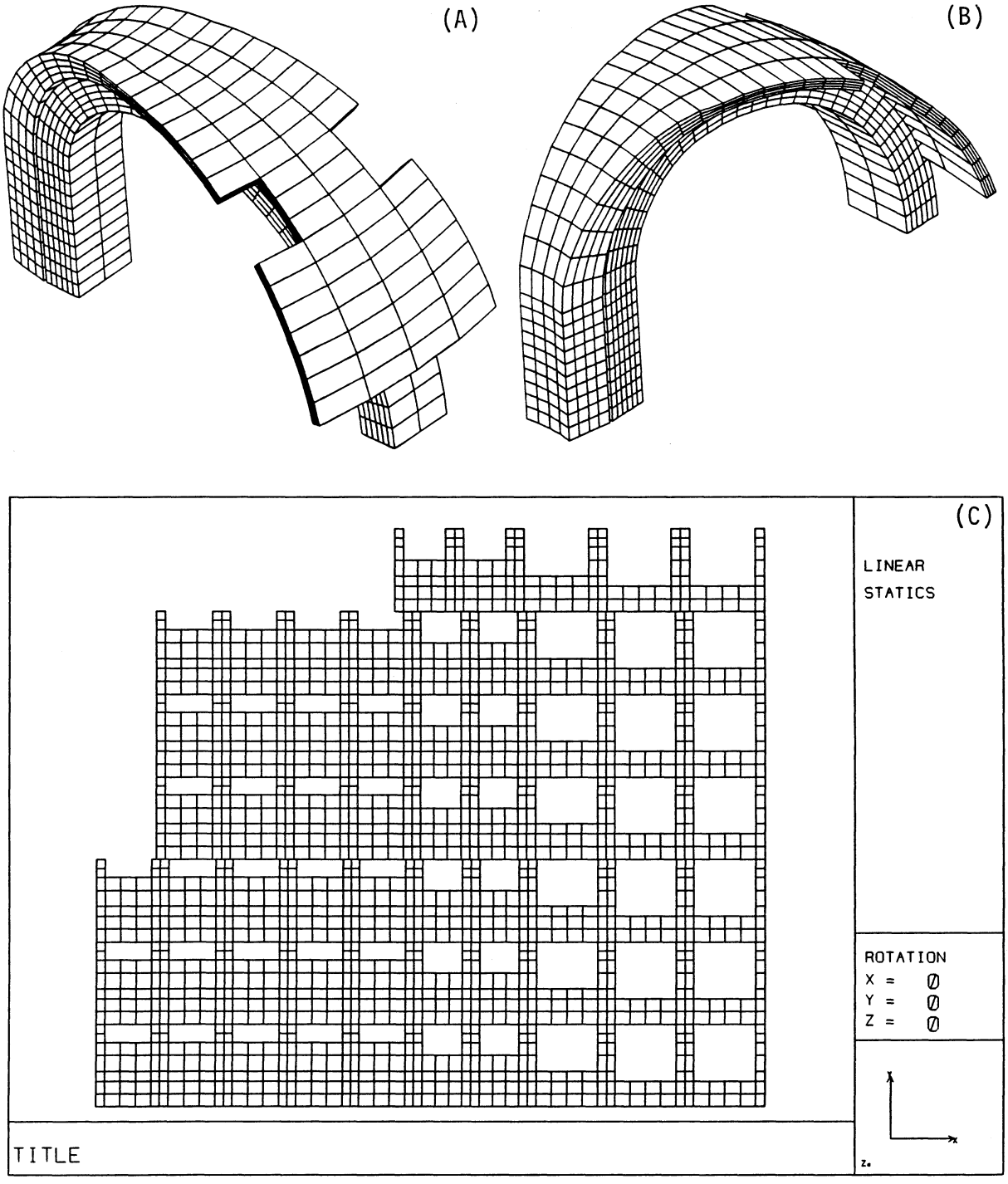

Figure 7.4-3. The finite-element model of the ARIES-I TF coil and the support structure, shown with continuous shell configuration. Views from (A) outer and (B) inner radii; (C) separate model of the TF cross section.

can be seen in Fig. 7.4-3. In practice, friction will transfer some of the vertical tension in the coil to the bucking cylinder. The effects of allowing the bucking cylinder to carry some of the vertical loads will be discussed later.

The TF coil and top/bottom torque-shell structures are attached by keys running along their length in order to ensure transmission of the out-of-plane loads. The model assumes that the nodal points between the TF coil and the shells are merged at the symmetry plane of the wedge. This assumption results in the transfer of radial and vertical loads (in addition to toroidal loads) between the TF coil and the shells. The consequences of this assumption will be discussed below. We have not included the keys between the TF coil and the bucking cylinder in the model. In the results reported in this section, the coils react the out-of-plane loads in the TF outer leg across the mid-plane. Incorporating the bucking cylinder would substantially decrease the shears in the throat of the TF coil.

The bucking cylinder is separated from the top torque shell at a height of 2.7 m in order to allow for removal of the top shell from the machine during maintenance procedures. This separation prevents vertical loads generated in the horizontal leg from being partially transferred to the bucking cylinder through the outer shell. It is possible to transfer out-of-plane shears through this interface by setting keys between the shell and the bucking cylinder, but this has not been included in this model. The ports required for removal of the divertor targets have been included in the model. Also, in the outer region the shells are assumed to stop at a height of 1.5 m from the mid-plane. In this region, the coils themselves carry some of the shears from the out-of-plane loads.

The applied Lorentz loads are shown in Fig. 7.4-4. The out-of-plane loads are about an order of magnitude smaller than the in-plane loads, and although included in the figure, their behavior can not really be determined from these plots. These figures also show the coordinate system used, with y being vertical and x being radial. Lorentz forces are obtained from an analysis using grid points that are compatible across the force analysis model and the ANSYS model. This correspondence of the nodal arrangement facilitates communication of element centroid forces between the force code and ANSYS. We have assumed that the current density in the TF magnet is uniform in each grade (*i.e.*, the current has been smeared over the conductor, structure, stabilizer, insulation, and coolant). The toroidal field is self-consistently calculated using this current distribution. The out-of-plane loads have been calculated using the high-beta, high-flux linkage equilibria described in Sec. 7.5 (Table 7.5-III). The 2-D axisymmetric array of forces is appropriately factored to three arrays of forces at the three layers of nodes in the toroidal field. The mid-plane nodes have twice the magnitude of the edge nodal forces.

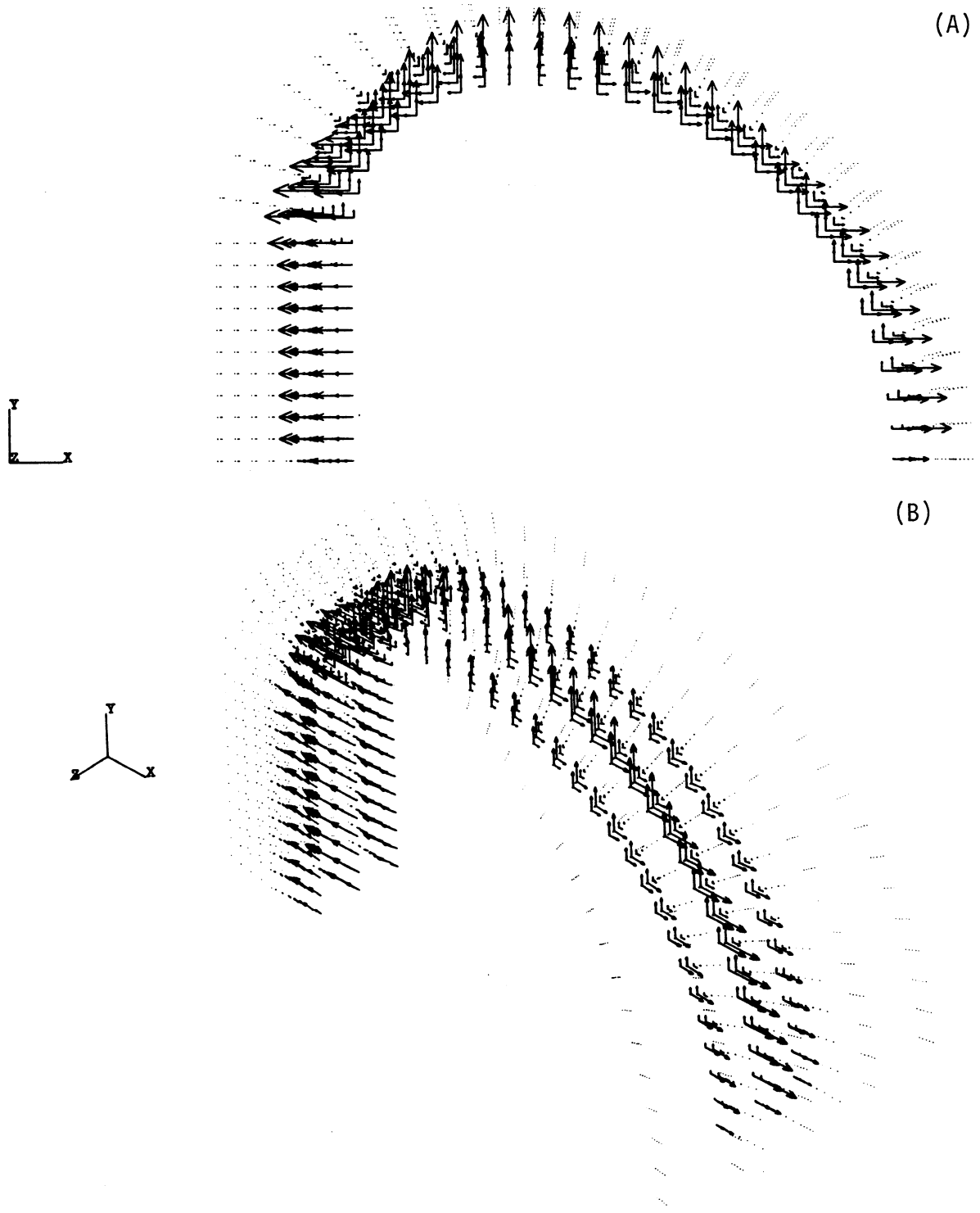

Figure 7.4-4. The finite-element model of the ARIES-I TF coil and the support structure. The node plots are with applied Lorentz loads (high-β equilibrium): (A) elevation view and (B) isometric view.

The constraints for the model are shown in Fig. 7.4-5. Cyclic symmetry constraints are accomplished by coupling nodes from symmetry boundary to symmetry boundary with degrees of freedom specified in a cylindrical coordinate system. Only the shell and the bucking cylinder have nodes at the cyclic symmetry plane [as shown in Fig. 7.4-5(A)]. The equatorial plane symmetry is modeled by setting the vertical displacement at the equatorial plane equal to zero. This is approximately accurate for the TF-coil inner-throat region if it is toroidally coupled to the bucking cylinder. The bend flexure of the TF-coil outer leg, as it takes the overturning torque, will produce rotation of planes in the TF coil at the equatorial plane about a machine major radius. These are accommodated by constraint equations that relate the vertical degrees of freedom of corresponding nodes at the equatorial plane on either side of the vertical mid-plane of the model. The TF coil and bucking cylinder are coupled radially. The remainder of the coil/shell interface is connected at the mid-plane by merging the nodes along the line of contact. ANSYS STIFF-45 eight-node solid elements are used throughout the model. The resulting displacements are shown in Fig. 7.4-6.

Figures 7.4-7 through 7.4-18 show the results of the finite-element analysis. The stresses of the TF coils are shown in Figs. 7.4-7 (radial, σ_x), 7.4-8 (vertical, σ_y), 7.4-9 (hoop, σ_z), 7.4-10 (torsional shear, τ_{yz}) and 7.4-11 (von Mises equivalent, σ_{eq}). The average vertical stresses in the throat of the TF coil on the mid-plane are $\sim$700 MPa. The radial stresses are $\sim$140 MPa, and the equivalent average stress on the mid-plane, with all the loads added, is $\sim$770 MPa. Accounting for space for gaps, cooling, and insulation, the average equivalent stresses (von Mises) in the TF coil are $\sim$840 MPa.

The loads on the bucking cylinder and the toroidal shell are shown in Figs. 7.4-12 (radial, σ_x), 7.4-13 (vertical, σ_y), 7.4-14 (hoop, σ_z), 7.4-15 (torsional shear, τ_{yz}) and 7.4-16 (equivalent, σ_{eq}). The toroidal stresses are $\sim$850 MPa. There is little net vertical load (because of the uncoupling) and small radial loads. The equivalent stresses are $\sim$900 MPa, lower than the ones chosen as allowable.

The thickness of the shell in the outer region of the magnet is 0.20 m. There are substantial stresses, σ_x and σ_z, on the shell because the TF coil and the shell have merged node points along the contact line. In reality, with keys aligned with the long dimension of the coil (to transmit the out-of-plane loads), there should be some slippage between the TF coil and the shell. This slippage should cause a small local increase of stresses in the top of the TF coil, with a corresponding large decrease of stresses in the shell (because of the relative sizes of the shell and the coil). Therefore, the shell will mainly carry shears resulting from the out-of-plane loads. These shear stresses, τ_{yz}, are small ($\sim$150 MPa maximum). Therefore, it should be possible to decrease the size of the

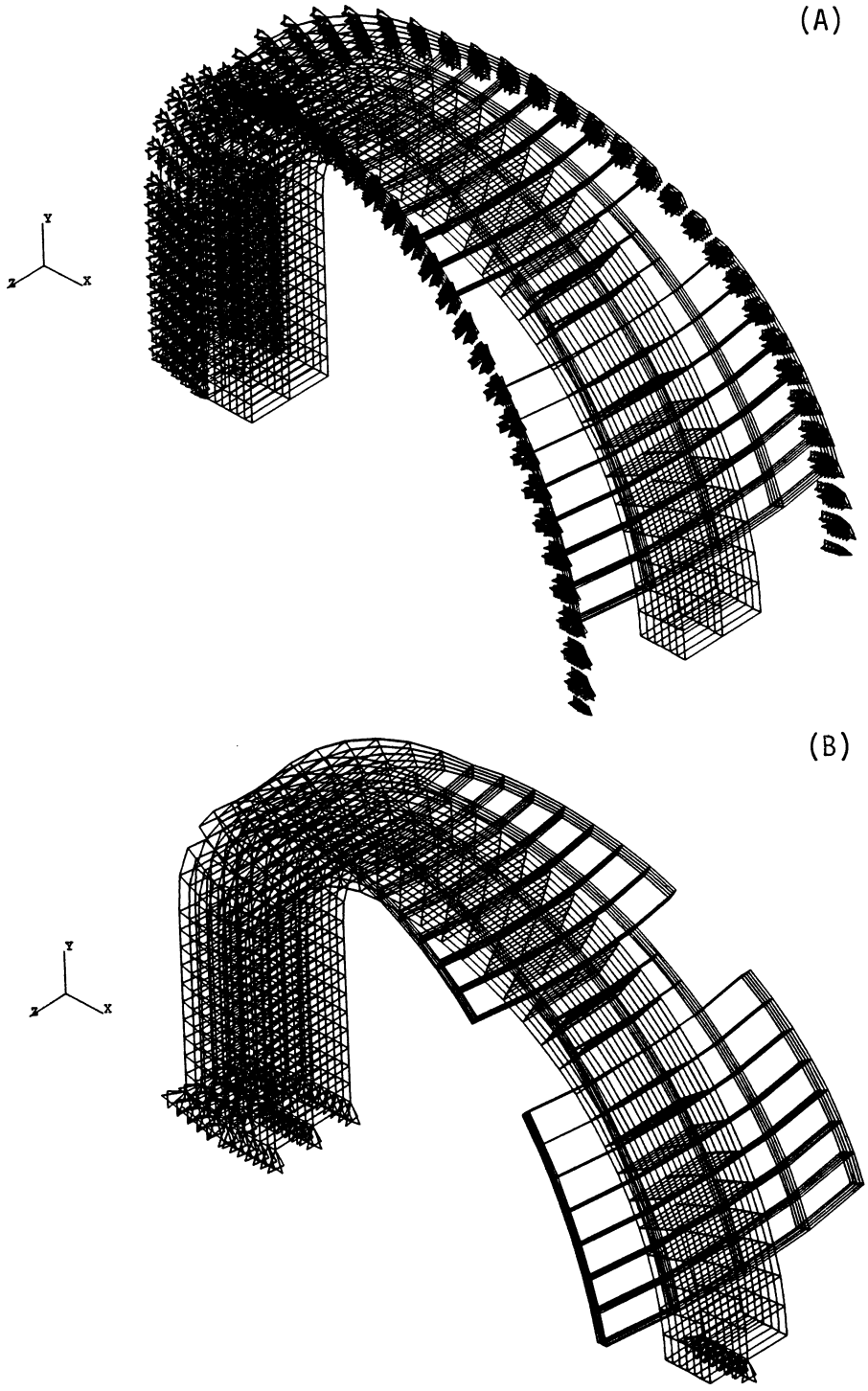

Figure 7.4-5. The finite-element model of the ARIES-I TF coil and the support structure. The node plots are with (A) cyclic symmetry constraints and (B) equatorial plane constraints (isometric views).

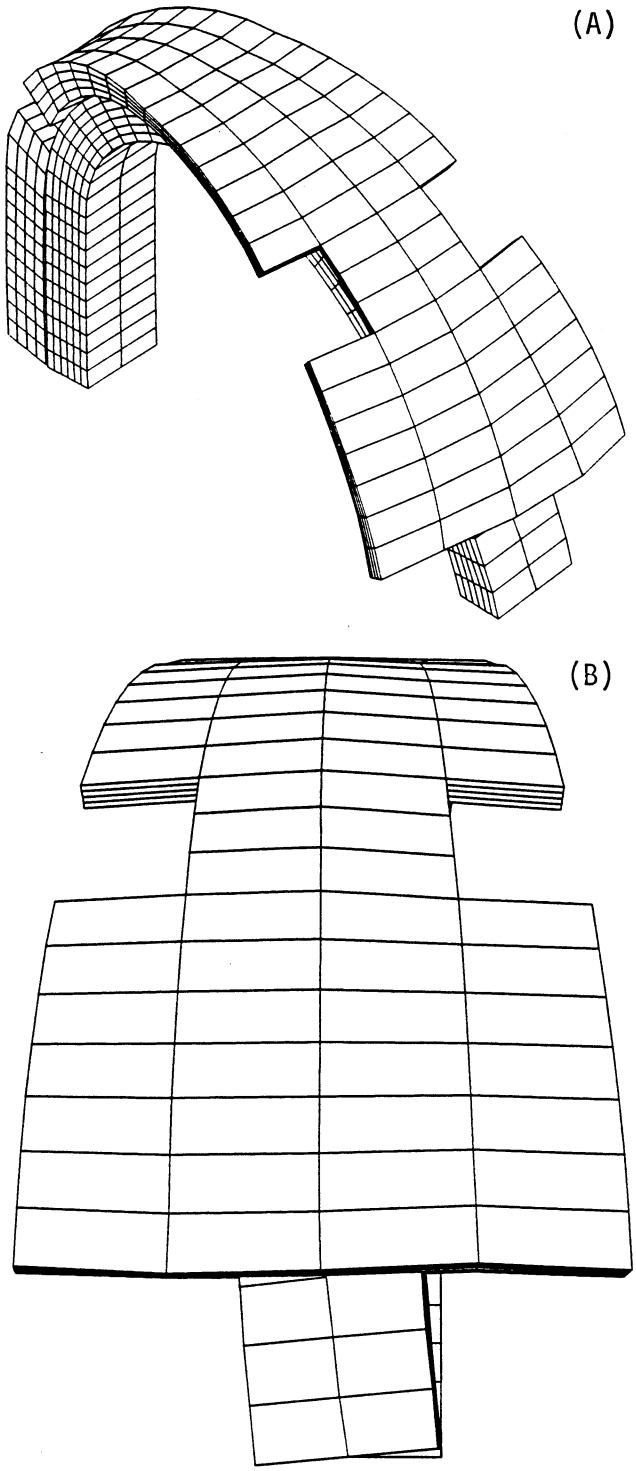

Figure 7.4-6. Displaced shape of the ARIES-I TF coil and the support structure (high-β equilibrium): (A) isometric view (B) end view (elevation).

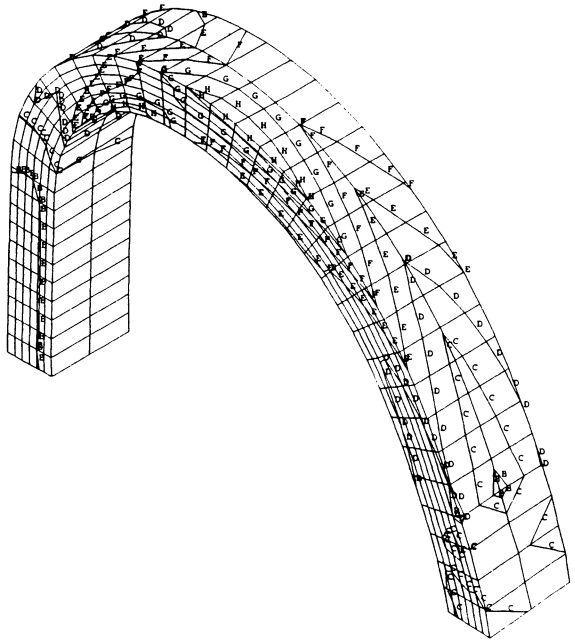

Figure 7.4-7. Contours of radial stress, σ_x, in ARIES-I TF coil (high-β equilibrium). Contours are labeled (all in MPa) as A = -215, B = -109, C = -4, D = 101, E = 207, F = 312, G = 417, and I = 628.

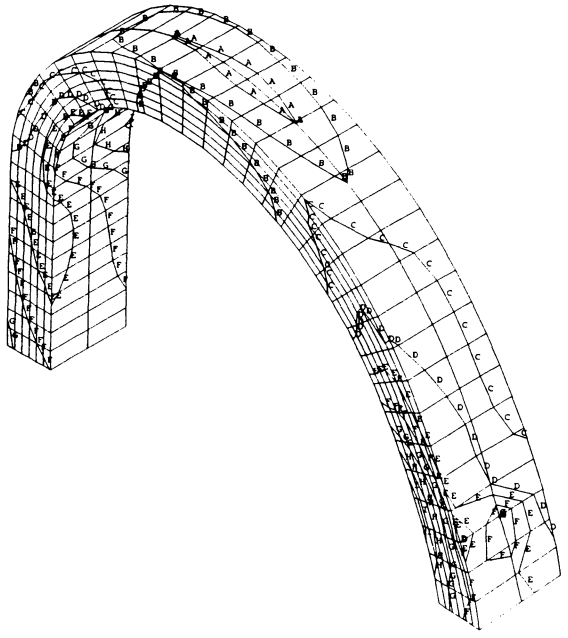

Figure 7.4-8. Contours of vertical stress, σ_y, in ARIES-I TF coil (high-β equilibrium). Contours are labeled (all in MPa) as A = -87, B = 39, C = 165, D = 291, E = 416, F = 542, G = 668, and I = 920.

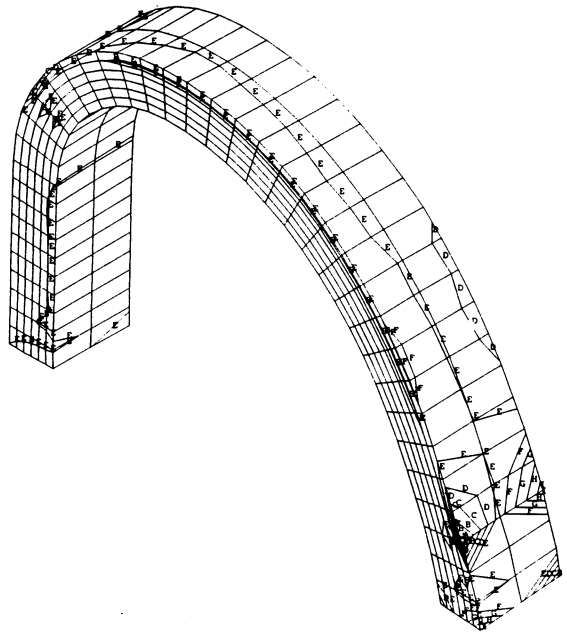

Figure 7.4-9. Contours of hoop stress, σ_z, in ARIES-I TF coil (high-β equilibrium). Contours are labeled (all in MPa) as A = –635, B = –483, C = –330, D = –178, E = –25, F = 127, G = 279, and I = 584.

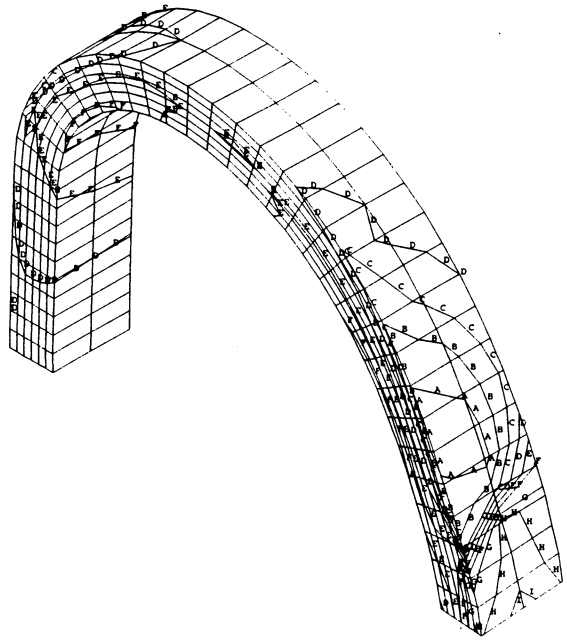

Figure 7.4-10. Contours of torsional shear stress, τ_{yz}, in ARIES-I TF coil (high-β equilibrium). Contours are labeled (all in MPa) as A = –130, B = –93, C = –58, D = –22, E = 13, F = 49, G = 84, and I = 155.

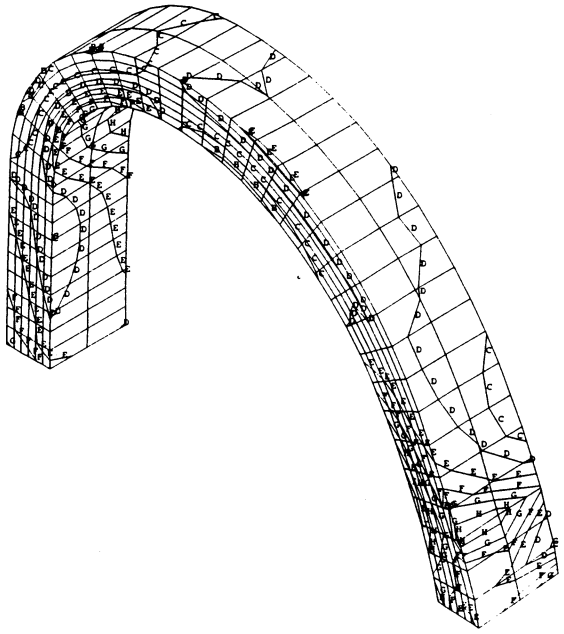

Figure 7.4-11. Contours of von Mises stress, σ_{eq}, in ARIES-I TF coil (high-β equilibrium). Contours are labeled (all in MPa) as A = 156, B = 265, C = 374, D = 483, E = 592, F = 701, G = 811, H = 920, and I = 1030.

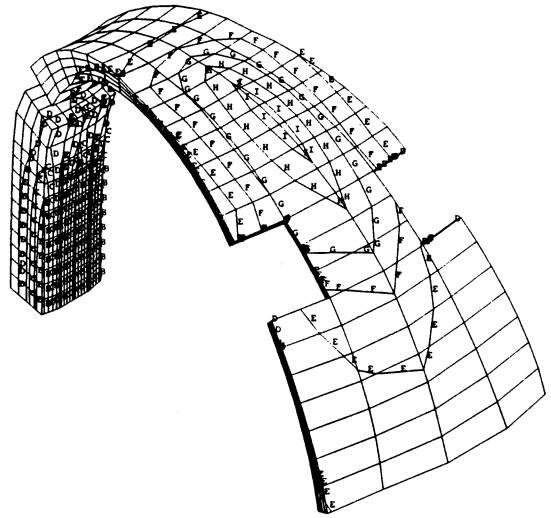

Figure 7.4-12. Contours of radial stress, σ_x, in ARIES-I TF-coil support structure (high-β equilibrium). Contours are labeled (all in MPa) as A = –555, B = –400, C = –244, D = –89, E = 66, F = 222, G = 377, and I = 688.

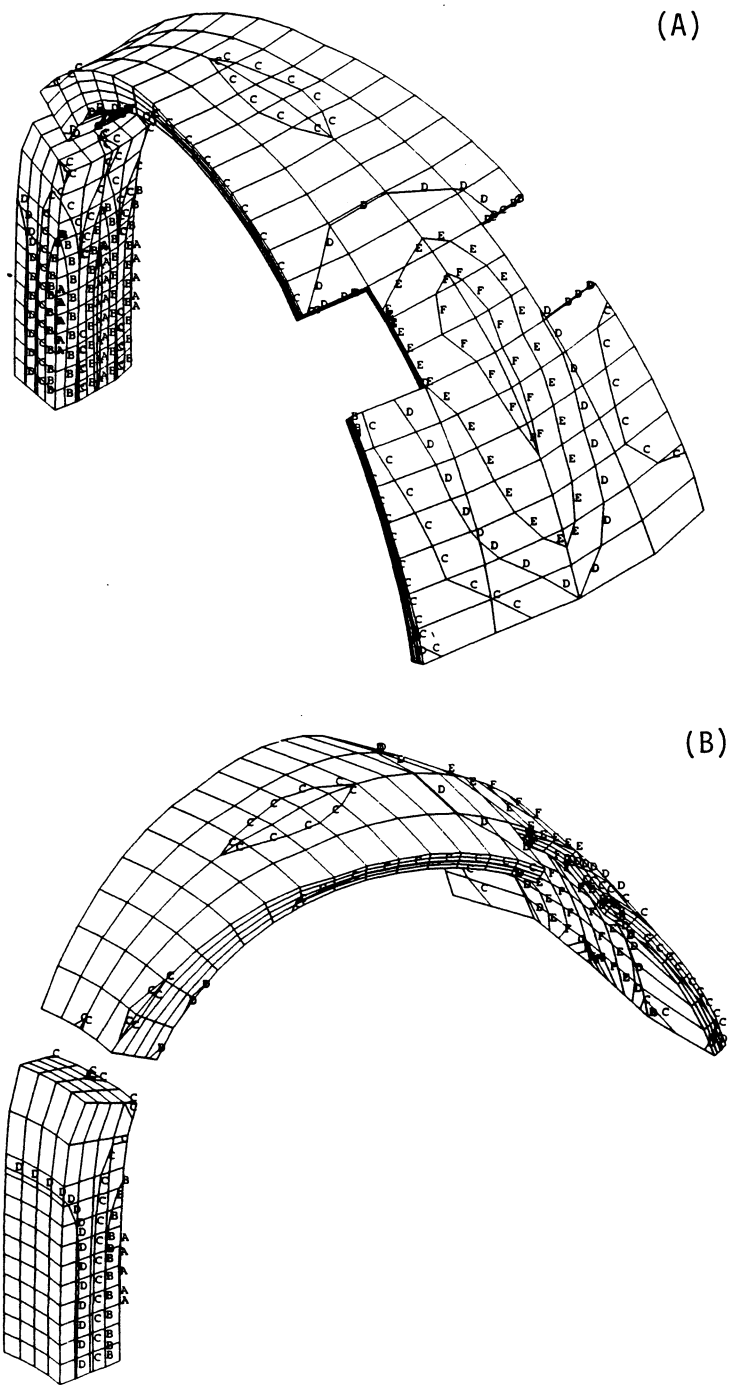

Figure 7.4-13. Contours of vertical stress, σ_y, in ARIES-I TF-coil support structure (high-β equilibrium) with views from (A) outer radius and (B) inner radius. Contours are labeled (all in MPa) as A = -223, B = -126, C = -28, D = 69, E = 166, F = 263, G = 361, and I = 555.

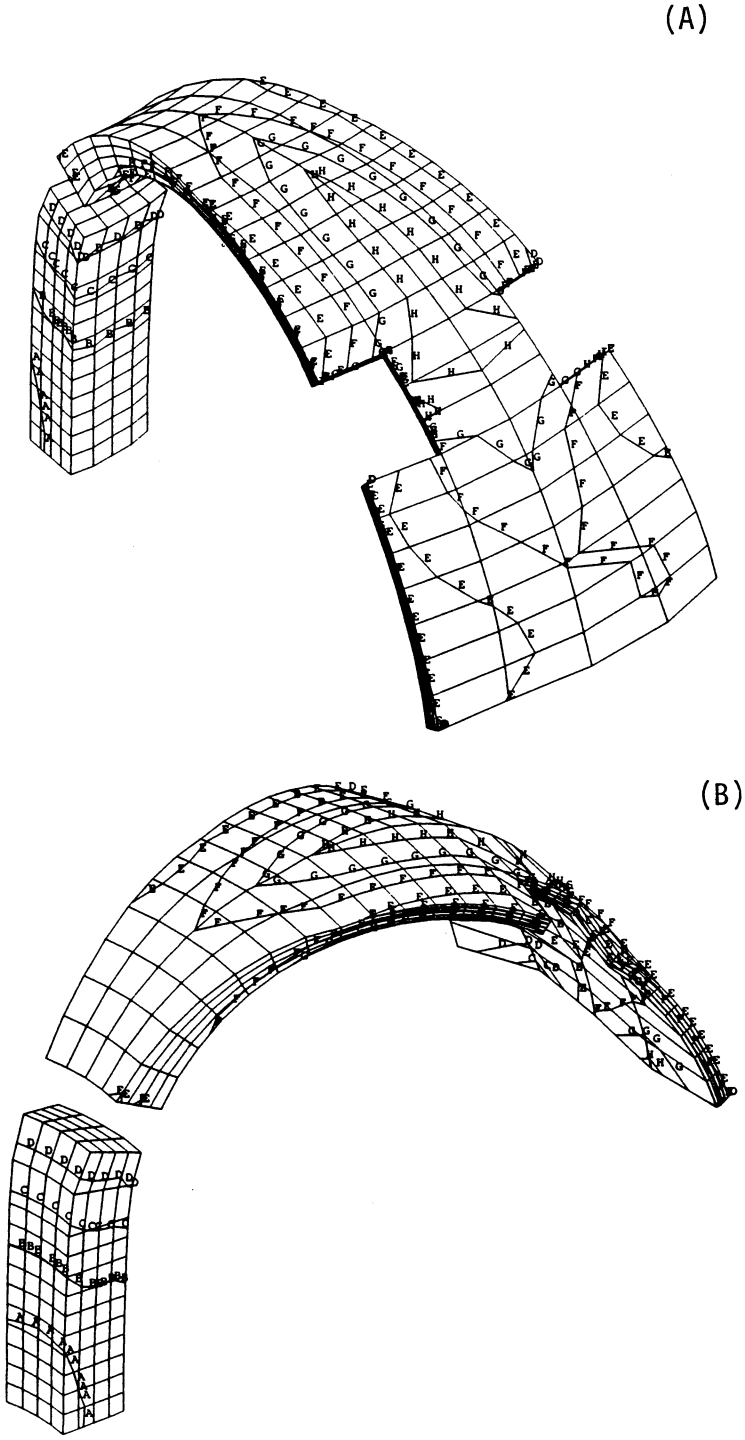

Figure 7.4-14. Contours of hoop stress, σ_z, in ARIES-I TF-coil support structure (high-β equilibrium) with views from (A) outer radius and (B) inner radius. Contours are labeled (all in MPa) as A = -903, B = -705, C = -506, D = -309, E = -110, F = 88, G = 286, and I = 682.

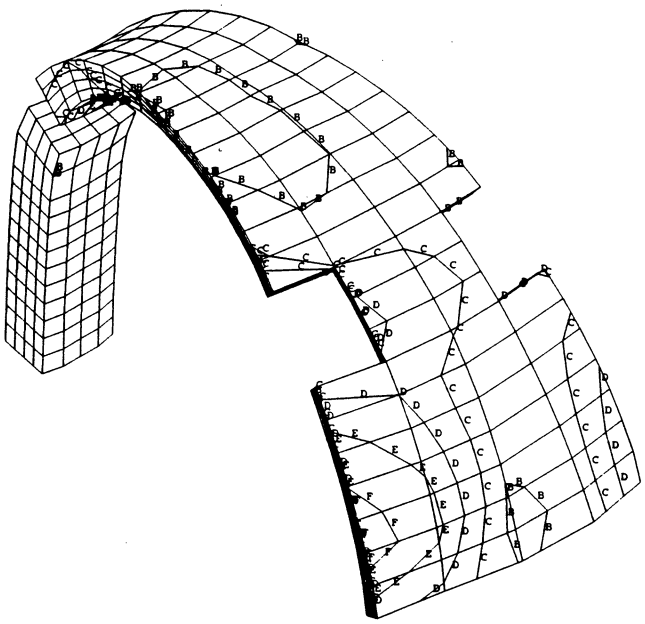

Figure 7.4-15. Contours of torsional shear stress, τ_{yz}, in ARIES-I TF-coil support structure (high-β equilibrium). Contours are labeled (all in MPa) as A = -55, B = -7, C = 41, D = 89, E = 137, F = 185, G = 233, and I = 329.

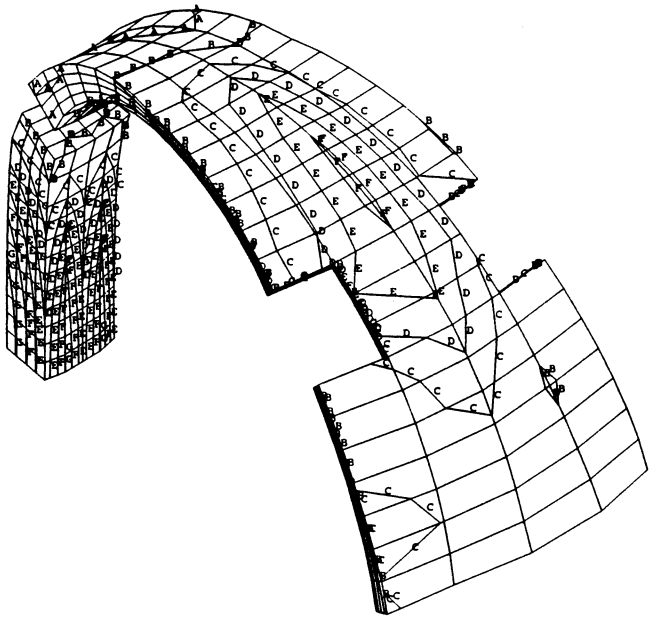

Figure 7.4-16. Contours of von Mises stress, σ_{eq}, in ARIES-I TF-coil support structure (high-β equilibrium). Contours are labeled (all in MPa) as A = 112, B = 254, C = 395, D = 534, E = 677, F = 818, G = 960, H = 1100, and I = 1242.

shells (caps) and our calculations of the weights of the different sections reflect a smaller size.

Figure 7.4-17 shows the resulting vertical stresses if the toroidal shell is assumed to be continuous with the bucking cylinder. The result is a net vertical stress in the bucking cylinder of about $\sigma_y \sim 300$ MPa. The vertical stresses in the throat of the magnet are decreased by about ~370 MPa to ~300 MPa, as shown in Fig. 7.4-18. The decrease in TF-coil vertical load is similar to the increase in the bucking cylinder load because the cross-sectional areas of both are similar. If a friction coefficient of 0.25 is used, the maximum value of the vertical stress of the bucking cylinder is ~150 MPa. Therefore, there must be some slippage between the TF coil and the bucking cylinder during energizing.

If the vertical stress of ~150 MPa is included in the bucking cylinder, then the equivalent stresses there increase to 1050 MPa, slightly larger than the allowable. The stresses in the TF coil decrease by about the same amount. The overstressing of the bucking cylinder could be remedied by increasing the bucking thickness of the cylinder slightly (~5%), a change causing little impact since the central ohmic-heating solenoid is not very demanding in ARIES-I (Sec. 7.5). In this case, the equivalent stresses in the TF coil would decrease to $\lesssim$ 700 MPa.

In conclusion, the finite stress analysis presented in this section shows that the stresses are slightly less than the approximate calculations done for Table 7.4-III. The coil and the bucking cylinder are within the allowable ranges.

7.4.3.2. Cryostats

Another important component from the maintenance point of view is the cryostat for the TF coils (Sec. 11). Instead of a large cryostat for the entire device, each coil has its own cryostat with two kinds of exterior surfaces. The first, occurring over the entire bore surface and some of the sides and outer surface, is the conventional type and the vacuum vessel is the visible component. The inward progression is the super-insulation and heat-shield layers within the vacuum, followed by a structural helium vessel and conductor matrix (or a matrix containing small-scale helium confinements such as tubes with the case being only structural).

The second type of exterior surface is visible and exposes the face, completely uninsulated, of the helium vessel or other major structural case. At the periphery of this face, a G10 plate connects the edges of the conventional exterior surface and the visible cryogenic components, forming a continuous flat face. Although this face is vacuum

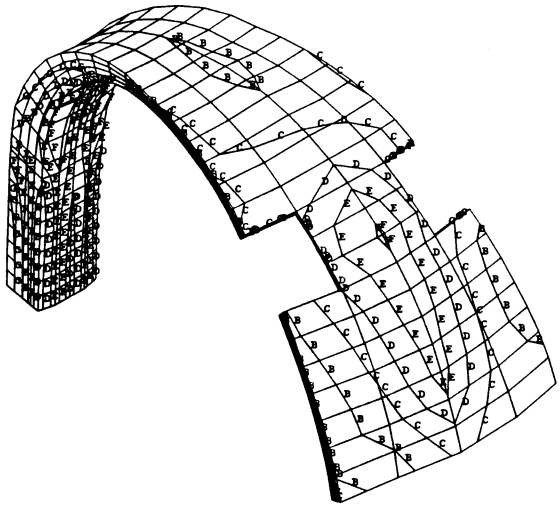

Figure 7.4-17. Contours of vertical stress, σ_y, in ARIES-I TF-coil support structure with bucking cylinder attached to the shell (high-β equilibrium). Contours are labeled (all in MPa) as A = –120, B = –34, C = 52, D = 138, E = 224, F = 310, G = 396, and I = 569.

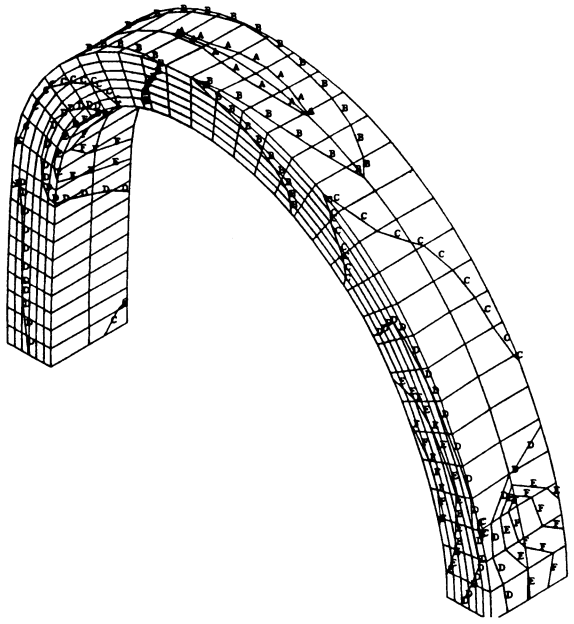

Figure 7.4-18. Contours of vertical stress, σ_y, in ARIES-I TF-coil with bucking cylinder attached to the shell (high-β equilibrium). Contours are labeled (all in MPa) as A = –85, B = 46, C = 176, D = 307, E = 437, F = 568, G = 698, and I = 959.

sealed, the magnet is not operable in this face-exposed condition because the matrix is not coolable with one face of its casing exposed to air. For magnet operation, each of these exposed faces must butt against an identical face in an adjacent fusion-power-core module, the bucking cylinder, or the torque shells. After the faces are aligned, the cryostat is evacuated and cool-down can begin. A typical TF coil with the interface surface is shown in Fig. 7.4-19.

Application of this new, cold-face concept eliminates the need to carry very large loads from cold to warm structural elements. When the heat leakage resulting from out-of-plane forces is calculated on the basis of cold-to-warm structure requirements, it is 10 times higher for a conventional design than for the proposed ARIES-I cold-face cryostat system. Moreover, because the cryostat system also deals with the center-post butting forces, the total benefit would be several times larger (*i.e.*, a factor of 50 over conventional design). Additionally, at least 0.15 m of space on each of the coil cross-section dimensions is saved. The use of the cold-face cryostat gives a new capability to avoid heat leak and allow for TF-coil removal. This cold-face interface concept, however, requires the machining of large components with more precision than is necessary for a conventional design.

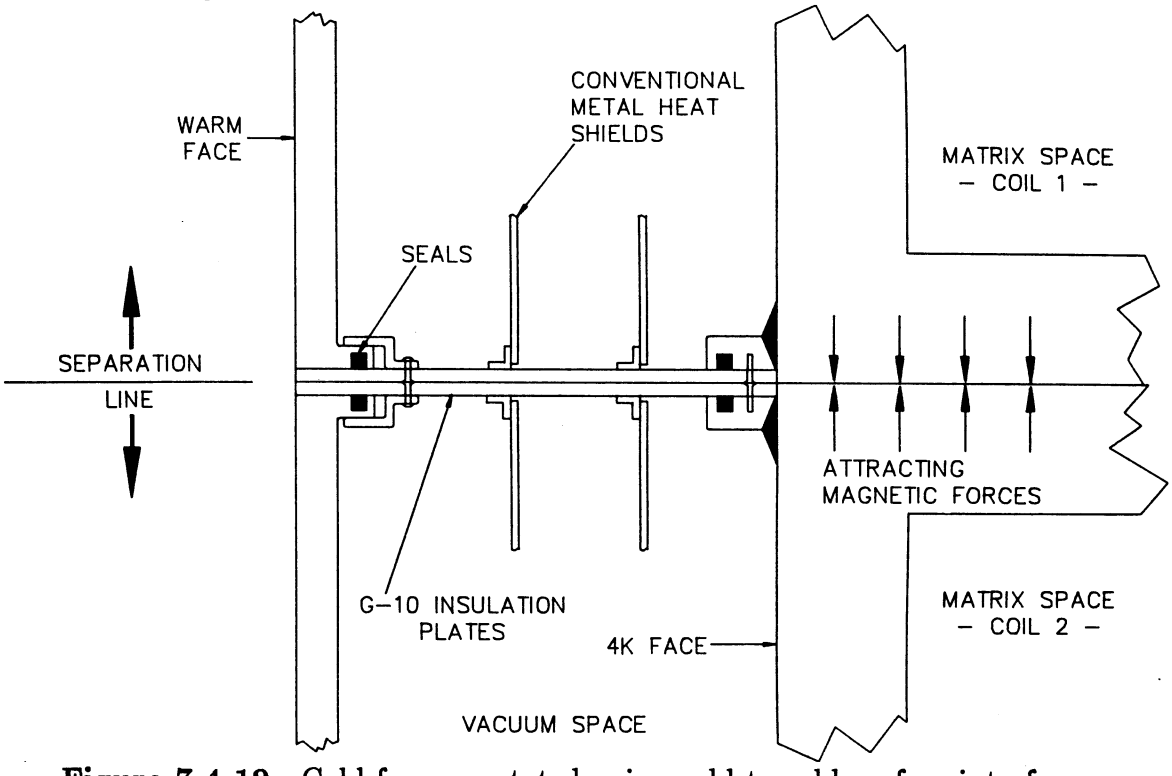

Figure 7.4-19. Cold-face cryostat showing cold-to-cold surface interface.

7.4.3.3. Design of a 24-T coil

During the scoping phase of the ARIES-I study, the feasibility of high-field TF magnets which are based on the latest laboratory achievements was investigated. This research effort resulted in the design of a 24-T (peak field) TF coil using $Nb_3(A\ell,Ge)$ superconductor. Further analysis, however, showed that because $Nb_3(A\ell,Ge)$ is presently only available in the form of tape conductors, losses in the TF coils during the disruption may cause the TF coils to quench. As a result, the reference ARIES-I design uses multifilamentary Nb_3Sn superconductor and achieves a peak field of 21 T at the coil. In this section, designs of two 24-T coils utilizing $Nb_3(A\ell,Ge)$ superconductors are presented, one using isotropic structural material (similar to the ARIES-I reference design) and one with fiber-reinforced materials. The cross sections of the TF-coil inner legs for the two designs are shown in Fig. 7.4-20.

Design of the composite material for the 24-T TF-coil plate requires selection of the carbon fiber properties (strength *versus* stiffness trade-off, Fig. 7.2-7), the fiber orientation, and the fiber volume fraction, k_f. For the TF-coil inner leg, the fibers are oriented vertically so that they support most of the vertical tensile load; the steel matrix will support the radial compressive load. The fiber properties and volume fraction are chosen such that the radial build of the coil and the composite failure parameter, G, are both minimized, as is illustrated in Fig. 7.4-21. The material properties selected for the design are given in Table 7.4-IV, the resulting composite design properties are in Table 7.4-V, and the resulting stress distribution is in Table 7.4-VI.

Table 7.4-VII compares the designs of the high-field grades for the two structural material options. Note that the superconductor J_c and T_c are determined at the highest-field point for the particular grade, while the structural material requirements are determined at the lowest-field point due to the buildup of radial load. The design methodology for the multifilamentary wire conductors is essentially the same as that for the tape conductor, with results shown in Table 7.4-VIII. For $B < 18$ T, the design is dominated by the structural material requirement (compare t_{plate} to w_{groove} and the plate area to the cable space area) and the impact of very high-strength composites is clearly evidenced. If the allowed stress is limited to 1 GPa, then $s_{rad} > 12$ cm and $h_{cond} > 11$ cm is required in the low-field region, resulting in large bending strain during winding. This leads to degradation of J_c and a potential for mechanical failure of the superconducting filaments at the outermost radius of the conductor where the bending is maximum. When a high-strength composite structure is used, however, the largest conductor is 5.76 cm in the bend direction, and the largest multifilamentary conductor is 5.03 cm. This is more than a 50% reduction in bending.

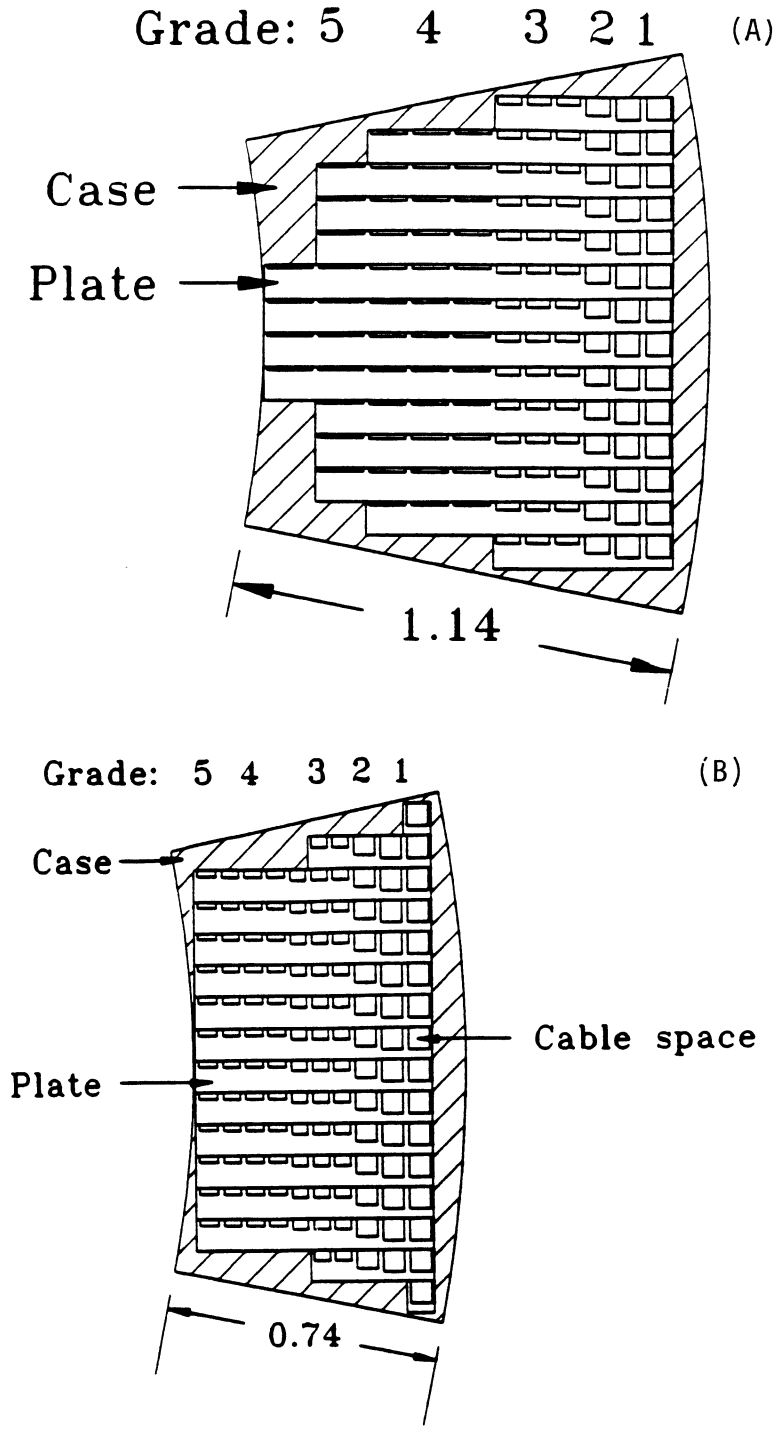

Figure 7.4-20. The cross section of the inner leg of 24-T TF-coil design with (A) isotropic steel and (B) composite structural material.

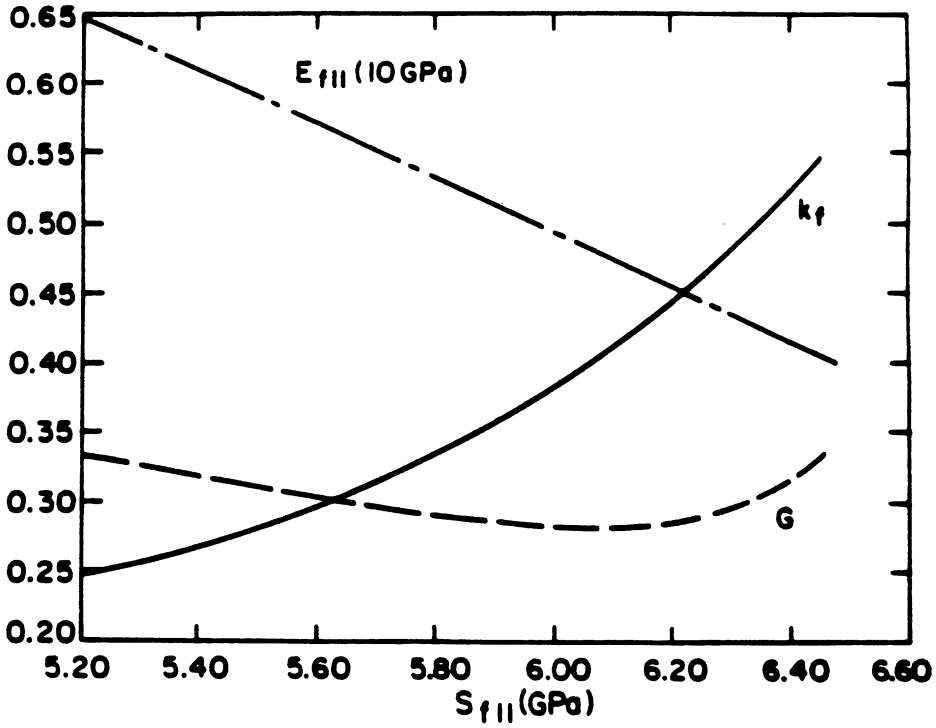

Figure 7.4-21. The optimized values of the composite failure parameter, G, and C fiber fraction, k_f, and modulus, $E_{f||}$, as functions of C fiber strength, $S_{f||}$, for the 24-T coil design.

Table 7.4-IV.
Material Properties for 24-T TF Coil

C fiber strength, vertical, $S_{f11,T}$ (GPa)	5.9
C fiber modulus, vertical, E_{f11} (GPa)	513
C fiber modulus, radial, E_{f22} (GPa)	9.6
Incoloy strength, $S_{m,T}$ (GPa)	2.0
Incoloy yield stress, $\sigma_{m,y}$ (GPa)	1.5
Incoloy modulus, E_m (GPa)	207
Incoloy strain to failure, $\epsilon_{ml,T}$	23%

Table 7.4-V.
Composite Design Properties for 24-T TF coil

C fiber fraction, k_f	35.6%
Incoloy fraction, k_m	64.4%
Void fraction, k_v	5.0%
Composite modulus, vertical, E_{c11} (GPa)	300
Composite strength, vertical tension, $S_{c11,T}$ (GPa)	2.9
Composite strength, radial compression, $S_{c22,C}$ (GPa)	1.2
Failure parameter, G	0.284

Table 7.4-VI.
Stress Distribution for 24-T TF Coil

Composite stress, vertical, $\sigma_{c11,T}$ (MPa)	877
Composite stress, radial, $\sigma_{c22,C}$ (MPa)	−373
C fiber stress, vertical, $\sigma_{f11,T}$ (MPa)	1500
C fiber equivalent stress (Tresca), $\sigma_{f,Tresca}$ (MPa)	1873
Incoloy stress, vertical, $\sigma_{m11,T}$ (MPa)	605
Incoloy equivalent stress (Tresca), $\sigma_{m,Tresca}$ (MPa)	978
Composite vertical strain, $\epsilon_{c11,T}$	0.29%

Table 7.4-VII.
Design Parameters
of Tape Conductor Sections of the 24-T TF Coil

Grade	1		2	
Field range (T)	$24 > B > 20.5$		$20.5 > B > 18$	
	Steel	Composite	Steel	Composite
J_c (10^8A/m^2)	1.94	1.94	2.51	2.51
T_c (K)	8.9	8.9	10.6	10.6
s_{tor} (cm)	8.5	8.5	8.5	8.5
s_{rad} (cm)	7.7	7.5	7.8	7.5
t_{plate} (cm)	2.56	2.34	3.68	3.32
h_{cond} (cm)	5.96	5.76	6.12	5.75
w_{cond} (cm)	4.80	5.06	3.72	4.10
w_{tape} (cm)	2.40	2.53	1.86	2.05
w_{groove} (cm)	5.71	5.92	4.55	4.95
t_{ins} (cm)	0.2	0.2	0.2	0.2
f_{sc}	0.362	0.355	0.352	0.339
f_{st}	0.638	0.645	0.648	0.661
Areas (10^{-4}m^2)				
Superconductor	10.3	10.3	8.0	8.0
Stabilizer	18.2	18.8	14.8	15.6
Conductor	28.6	29.2	22.8	23.6
Helium	5.4	4.9	5.0	4.9
Cable space	34.0	34.1	27.8	28.5
Plate	27.7	24.5	34.8	29.7
Insulation	3.2	3.1	3.2	3.1
Total	65.0	61.6	65.8	61.3

Table 7.4-VIII.
Design Parameters
of Multifilamentary Conductor Sections of the 24-T TF Coil

Grade	3		4		5	
Field range (T)	$18 > B > 11$		$11 > B > 4$		$4 > B$	
	Steel	Composite	Steel	Composite	Steel	Composite
J_c (10^8A/m^2)	4.98	4.98	31.4	31.4	46.5	46.5
T_c (K)	6.5	6.5	11.1	11.1	6.6	6.6
s_{tor} (cm)	8.5	8.5	8.5	8.5	8.5	8.5
s_{rad} (cm)	7.7	6.0	11.0	6.4	13.4	6.8
t_{plate} (cm)	6.14	5.46	7.36	6.48	7.52	6.54
h_{cond} (cm)	6.04	4.29	9.29	4.69	11.66	5.03
$w_{cond} = w_{groove}$ (cm)	2.07	2.87	0.98	1.89	0.76	1.72
t_{ins} (cm)	0.2	0.2	0.2	0.2	0.2	0.2
f_{sc}	0.342	0.348	0.076	0.078	0.053	0.054
f_{st}	0.658	0.652	0.924	0.922	0.947	0.946
Areas (10^{-4}m^2)						
Superconductor	4.0	4.0	0.64	0.64	0.43	0.43
Stabilizer	7.8	7.6	7.8	7.6	7.8	7.6
Conductor	11.8	11.6	8.4	8.2	8.2	8.0
Helium	0.74	0.74	0.67	0.66	0.66	0.65
Cable space	12.5	12.3	9.1	8.9	8.9	8.6
Plate	49.5	37.4	81.0	43.2	101.1	45.9
Insulation	3.2	2.9	3.9	3.0	4.5	3.1
Total	65.2	52.6	93.9	55.0	114.5	57.6

Global input parameters for the design are listed in Table 7.4-IX and resulting magnet parameters are in Table 7.4-X.

Table 7.4-IX.
Design Parameters of the 24-T TF Coil

Magnetic field (T)	23.75
I_{pack} (kA)	200
V_{max} (kV)	20
S_{max} (A^2 s/m^4)	5×10^{16}
Number of coils	16
Ripple on axis	0.15%
Ripple on edge	1.49%
Thermal contraction (from 293 to 4 K)	
Superconductor	2×10^{-3}
Stabilizer	3×10^{-3}
Plate	2×10^{-3}
Case	3×10^{-3}
Insulation	2×10^{-3}

Table 7.4-X.
Design Results for the 24-T TF coil

	Steel	Composite
Radial build (m)	1.14	0.74
J_{magnet} (MA/m^2)	21.4	28.5
J_{st} (MA/m^2)	220	226
E_{stored} (total, GJ)	133	126
E_{stored} (circuit, GJ)	4.1	3.9
Vertical stress, stabilizer (MPa)	744	707
Vertical stress, case (MPa)	865	1275
Area fraction (%)		
Superconductor	4.8	6.5
Stabilizer	11.4	15.4
Plate	56.3	49.7
Case	21.7	21.3
Helium	2.3	2.9
Insulation	4.0	4.6

7.5. POLOIDAL-FIELD SYSTEM DESIGN

The poloidal-field (PF) magnets are responsible for forming and shaping highly elongated plasmas during a long pulse to steady-state burn. In ARIES-I, all PF coils are external to the toroidal-field system and are superconducting, using internally cooled, cable-in-conduit conductor of ternary Nb_3Sn, as in ITER [26]. The design of the PF-magnet system does not share the feasibility and development issues of the toroidal-field system. Most of the PF magnets have relatively low fields and current densities. However, analysis of conductors used in ITER [26] has shown that less advanced superconductors, such as NbTi, do not provide any economic advantage over conductors that are designed to reasonable standards of energy and temperature margins and recovery from disturbance, as well as to the universal design criterion of satisfying a minimum fraction of conductor critical current. Ternary NB_3Sn is favored over binary because it has higher temperature margins even at the lower fields.

The poloidal-field system is designed to control an 11.3-MA plasma over a range of beta and internal inductance. It is not designed to provide full ohmic initiation and start-up, but is capable of providing a substantial fraction of the ohmic requirement with assistance from the radio-frequency (RF) current-drive system. A poloidal-field-system trade study led to the selection of a 22-V-s flattop capability. Since there is no quantitative flattop requirement, the design criterion was to stay within the flux swing regime in which cost increases very slowly with capability. The PF-coil set is described in Table 7.5-I.

7.5.1. Magnet Allowables

Design allowables for the superconducting PF magnets, which were established for ITER in 1989 [28], are listed in Table 7.5-II, along with suggested additional constraints on energy and power-balance criteria for recovery from disturbances. The ARIES-I poloidal-field-system design follows the ITER recommendations, with the exception that the Tresca membrane allowable stress is 800 MPa for ITER and 1000 MPa for ARIES-I. The tensile stress limit for ITER of 450 MPa is based on fatigue crack-growth limits in the pulsed tokamak experiment. Since ARIES-I is limited to under 100 cycles, fatigue is less limiting than the Tresca membrane and bending stresses in the conductor conduits. The ARIES-I coils are more conservative than those of ITER in that they are also designed for energy margins > 0.5 J/cm^3 and fractions of critical current in the well-cooled recovery regime.

Table 7.5-I.
ARIES-I PF-Magnet Winding-Pack Dimension

Coil	R (m)	dR (m)	Z (m)	dZ (m)	n_{turns}
PF1,U,L	2.2	0.75	±0.75	1.5	400
PF2,U,L	2.2	0.75	±2.25	1.5	400
PF3,U,L	2.2	1.0	±4.75	1.0	400
PF4,U,L	4.0	1.2	±6.4	1.2	500
PF5,U,L	12.5	0.75	±5.4	0.75	300
PF6,U,L	12.5	0.75	±2.4	0.75	100

Table 7.5-II.
ITER PF-Magnet Constraints Used for ARIES-I Design

$V_{terminal}$ (kV)	20
I_{cond} (kA)	50
B_{max} (T)	13.6
$\sigma_{Tresca\ membrane}$ (MPa)	1000
$f_{critical}$	0.6
$T_{max,dump}$ (K)	150
T_{margin} (K)	0.5
E_{margin}[(a)] (J/cm^3)	0.5
$f_{wellcooled\ recovery}$[(a)]	0.8

[(a)]Suggested values.

In Table 7.5-II, $f_{critical}$ is the maximum-allowable ratio of conductor current to critical current; $f_{wellcooled\ recovery}$ is the maximum ratio of conductor current to the current at the transition point between well-cooled and ill-cooled behavior during recovery from a disturbance; $T_{max,dump}$ is the maximum-permissible temperature in the winding pack following a coil dump; T_{margin} is the minimum-permissible temperature difference between the local conductor temperature and the current-sharing temperature during a scenario; and E_{margin} is the minimum-permissible local energy margin, defined as the volumetric energy needed to be deposited in the conductor metal that would result in heating the local helium reservoir to the current-sharing temperature.

New equations for critical current were derived by Miller [28] by reworking an interpretation of Suenaga's data on multifilamentary-Nb_3Sn conductor with titanium additions [27] into a form suitable to pulsed loss calculations. The form of these equations agreed upon for use in the ITER design may be found in Ref. [28] and are repeated below. The fractions of critical current are calculated at each point in a scenario, including the effects of strain in the superconductor and heating of the supercritical helium coolant. Critical fractions and margins are also recalculated after disruption simulations, because it is assumed that disruptions are capable of occurring at any time during a cycle.

The critical current density of any superconductor is defined as:

$$J_c(B,T,\epsilon) = \frac{C_0\,(1-t^2)^2\,(1-b)^2}{[B_{c2}(T,\epsilon)\,b]^{1/2}}\,, \tag{7.5-1}$$

where B is the local flux density, T is the temperature, ϵ is the longitudinal strain in the filaments from all effects combined, C_0 is a constant, and B_c and T_c are, respectively, the critical field and temperature. The normalized field, b, and the normalized temperature, t, are, respectively,

$$b \equiv \frac{B}{B_{c2}(T,\epsilon)}\,, \tag{7.5-2}$$

$$t \equiv \frac{T}{T_{c0}(\epsilon)}\,. \tag{7.5-3}$$

An empirical fit for the temperature dependence of critical flux density is

$$B_{c2}(T,\epsilon) = B_{c20}(\epsilon)\,(1-t^2)\left(1-\frac{t}{3}\right)\,, \tag{7.5-4}$$

with a strain dependence of

$$B_{c20}(\epsilon) = B_{c20m}\left(1-a\,|\epsilon|^{1.7}\right)\,, \tag{7.5-5}$$

$$T_{c0}(\epsilon) = T_{c0m}\left(1-a\,|\epsilon|^{1.7}\right)^{1/3}\,, \tag{7.5-6}$$

where $a = 900$ when $\epsilon < 0$ and $a = 1250$ when $\epsilon > 0$. For ternary Nb_3Sn, $B_{c20m} = 28$ T, $T_{c0m} = 18$ K, and $C_0 = 13,400$ (A/T-mm^2).

Forced-flow, internally cooled cables have two recovery regimes. In the well-cooled regime, almost the entire local enthalpy of helium in the conduit at constant density, between the bath temperature and the current-sharing temperature, is available for conductor recovery. The Schultz-Minervini design criterion predicts that the fraction of critical current at which the transition between the well- and ill-cooled regimes takes place should be:

$$f_{tr} = \left[\frac{P_w\, h\,(T_c - T_b)\, A_{cu}}{\rho\, I_{cond}^2}\right]^{1/2}, \tag{7.5-7}$$

where P_w is the wetted perimeter, $h \approx 800$ W/K-m^2 is the integral average heat-transfer coefficient during a recovery event, T_c is the superconductor critical temperature, ρ is the stabilizer resistivity, A_{cu} is the stabilizer cross-sectional area, and I_{cond} is the conductor current. To design in the well-cooled regime, the fraction of critical current selected should be some high fraction of the transition fraction (*e.g.*, $J/J_c = 0.8 f_{tr}$).

7.5.2. Volt-Second Capability

Trade studies showed that the design of the ARIES-I poloidal-field system is qualitatively different from that of pulsed tokamaks, such as ITER and CIT. Since there is no ohmic start-up, the design doesn't require maximization of volt-second capability. However, a design philosophy, which was used in some previous steady-state designs, that eliminated all volt-second capability in order to minimize cost was unnecessarily aggressive. Conventional methods for minimizing stored energy led to designs with unrealistically small fractions of metal in the coil winding packs. Furthermore, because of the flatness of the cost and energy minima, a significant amount of flattop and start-up volt-second capability can be included for a small increase in coil costs. Given the probable need to handle off-normal conditions, a modest flattop capacity of 22 V-s was selected. This includes a capability of flattop at full current for either high or low beta plasmas in order to ensure the ability to heat and quench the burning plasma. Additional constraints on overall metal fraction and on the ratio of copper to non-copper were added to ensure coil fabricability.

In order to evaluate the capabilities of the poloidal-field system, MHD equilibria were generated over a range of flux linkages at high and low beta. The sensitivity of performance figures to flux linkage over this range is illustrated in Fig. 7.5-1, which shows

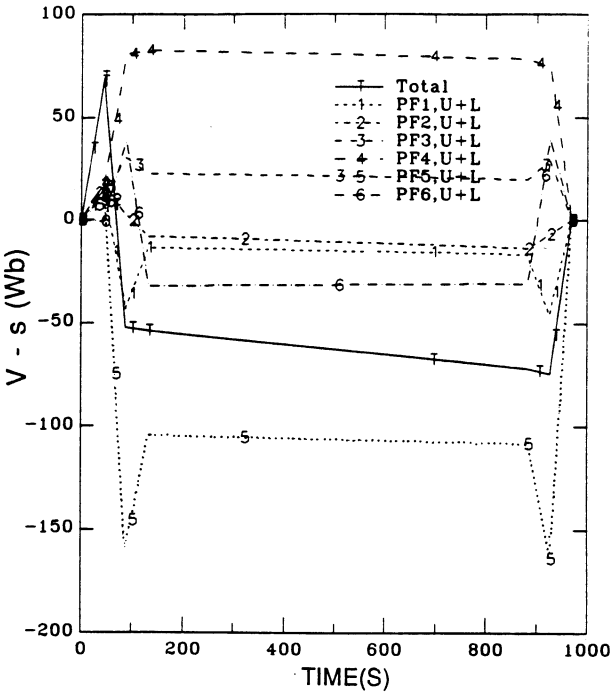

Figure 7.5-1. Volt-second swing capability of ARIES-I poloidal-field system for possible pulsed scenario.

the relation of actual to allowable performance parameters in the six pairs of PF coils at low beta for a low-beta, full-current plasma. The low beta limits are shown because they proved to be more limiting than high beta for most of the coils and materials. The peak values of each feasibility parameter over the selected flattop range of −52 to −74 V-s are listed in Table 7.5-III. In the table, $f_{c,max}$ is the maximum ratio of the conductor current to critical current; $f_{Jprot,max}$ is the ratio between the conductor current and the maximum current limited by protection; $T_{head,min}$ is the minimum-temperature headroom between the current-sharing temperature and the initial helium temperature, on the basis of field and current, in the absence of detailed knowledge of transient heating and cooling; $E_{head,min}$ is the minimum volumetric energy in the conductor metal headroom between the helium enthalpy at the initial temperature and at the current-sharing temperature, in the absence of detailed knowledge of transient heating and cooling; f_{tr} is the maximum ratio of the conductor current to the current at the transition between well-cooled and ill-cooled behavior during recovery from transient disturbances; $\sigma_{Tr,ext}$ is the maximum Tresca stress in the conductor conduits, accounting for the forces from the external coils, as in the central solenoid stack; $\sigma_{t,mem}$ is the maximum tensile-membrane stress in the conduit; and I_{coil} is the current in the corresponding coil at the specified conditions.

Table 7.5-III.
PF-Coil Actuals Over Design Range of Full Current Flattop

Coil	B_{max} (T)	$f_{c,max}$	$f_{Jprot,max}$	$T_{head,min}$ (K)	$E_{head,min}$ (J/cm^3)	f_{tr}	$\sigma_{Tr,ext}$ (MPa)	$\sigma_{t,mem}$ (MPa)	I_{coil} (MA)
				High-β Equilibrium					
PF1,U	2.9	0.05	0.06	7.94	10.8	0.14	215	25	-5.1
PF2,U	3.8	0.09	0.02	7.11	7.2	0.13	260	0	-3.6
PF3,U	10.4	0.13	0.18	3.39	1.4	0.40	651	524	14.6
PF4,U	9.3	0.51	0.36	2.24	1.3	0.87	751	862	24.5
PF5,U	4.6	0.24	0.40	5.66	3.6	0.33	548	533	-8.1
PF6,U	1.5	0.27	0.03	6.82	6.0	0.14	980	902	-1.8
				Low-β Equilibrium					
PF1,U	8.7	0.53	0.29	2.27	2.8	0.78	969	336	-16.3
PF2,U	7.1	0.26	0.03	1.79	2.8	0.26	811	244	0.98
PF3,U	12.7	0.30	0.27	1.70	0.6	0.76	947	777	19.9
PF4,U	9.0	0.46	0.35	2.53	1.5	0.81	921	749	23.9
PF5,U	6.6	0.55	0.69	2.74	1.6	0.64	939	912	-12.4
PF6,U	1.9	0.38	0.03	5.62	4.8	0.18	715	0	2.2

The selected design was then evaluated to have a capability of volt-seconds for initiation, but initiation requirements were not used to select material fractions. The degree of initiation and start-up capability of ARIES-I is somewhat arbitrary because of the considerable amount of current-drive power available to assist and the steady-state flattop capability. The design process described above led to a reference poloidal-field-system design with an end-of-burn capability of 144 V-s, which can also provide 60% of the volt-seconds needed for start-up without current-drive assist, and a 22-V-s full-current flattop at high and low beta, as shown in Fig. 7.5-1.

The ARIES-I reactor operates at steady state and has a modest plasma current of 11.3 MA. The peak field in the poloidal-field system is only 12.8 T, as shown in Fig. 7.5-2, and pulsed losses in the poloidal-field system are modest in comparison with those of the toroidal-field system because of the much smaller volume of superconductor required. The peak poloidal-field energy of 17.8 GJ, dominated by low-β plasma equilibrium requirements, is comparable to that of ITER. Because of the slow charging of the coils, the peak power and power supply requirements are modest, comparable to those of JET, and less expensive because of the absence of on-site pulsed-power facilities. A SAVAR power-factor correction-control circuit [29] is used in order to prevent large circulating reactive power in the utility line that feeds the poloidal-field circuits.

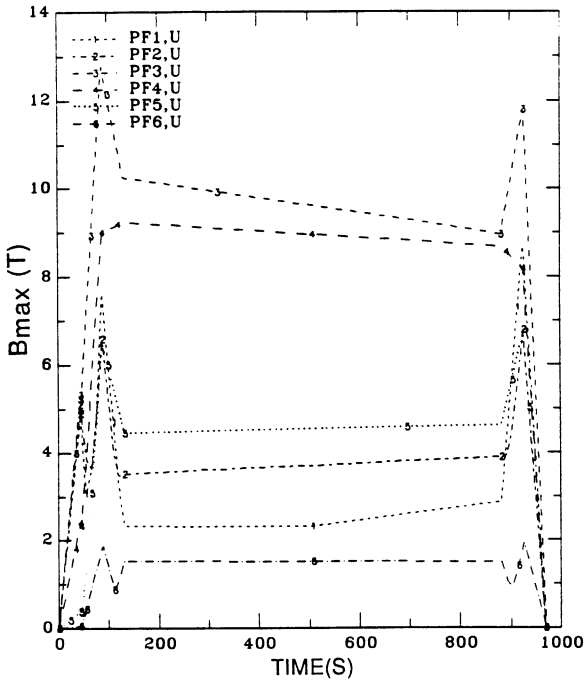

Figure 7.5-2. Maximum flux densities in each PF coil for possible pulsed scenario.

7.5.3. Poloidal-Field Scenarios

The ARIES-I reactor operates at steady state. However, at some definite interval (*e.g.,* once a year), it must initiate plasma, ramp up plasma current, heat to ignition, burn, quench, and ramp down the plasma current, just as would a pulsed tokamak. The ARIES-I reactor also has to be designed for a finite probability of disruption, although that probability will be considerably smaller than that for near-term experimental tokamaks. The design approach to ARIES-I is that it should be able to absorb the losses, forces, and voltage transients from a disruption at any time during a startup or shutdown.

After determining the poloidal-field burn operating range and initiation capability, a poloidal-field scenario was developed to cover the plasma and coil states before and after initiation, ramp-up, heating, burn, quench, and ramp-down. The amount of time taken to ramp up the plasma is a soft design compromise between the additional costs of magnet power-supply equipment and the costs of equipment to handle additional power and reactive power in the poloidal-field system; the same considerations apply for the RF current-drive system that would be used to assist the poloidal field. The basic design philosophy was to maximize the use of whatever capability had already been selected for flattop. Since the poloidal-field system is capable of slightly more than half of that required for a fully ohmic initiation and start-up, the time for each event is similar to that in pulsed reactor designs, such as ITER [26].

The energy requirements for the reference design are shown in Fig. 7.5-3(A). The poloidal-field system has a peak stored energy of 17.8 GJ at the end of start-up and a high-β peak of 12.8 GJ at the beginning of burn, as shown in Fig. 7.5-3(B). The peak power of 739 MW during start-up, shown in Fig. 7.5-3(A) could be reduced by a slower current ramp. However, with the current design, the power supply cost is driven more strongly by the coil ampacity and the utility volt-ampere reactive requirements than by instantaneous real power.

In a workshop on cryogenic refrigeration and power supplies, which was held during the 1989 ITER summer session, it was indicated that site selection was more strongly determined by negative and reactive power than by positive power. The overall ITER power requirements are modest when compared with pulsed copper tokamaks, comparable to JET, and considerably less than CIT. The overall ARIES-I power requirements are somewhat lower than those for ITER. However, the most common solution used by experimental fusion laboratories for obtaining pulsed rotating energy from motor-generator-flywheel sets is undesirable for ARIES-I because of much higher stored energy, poor utilization of infrequently pulsed power supplies, and stringent requirements on

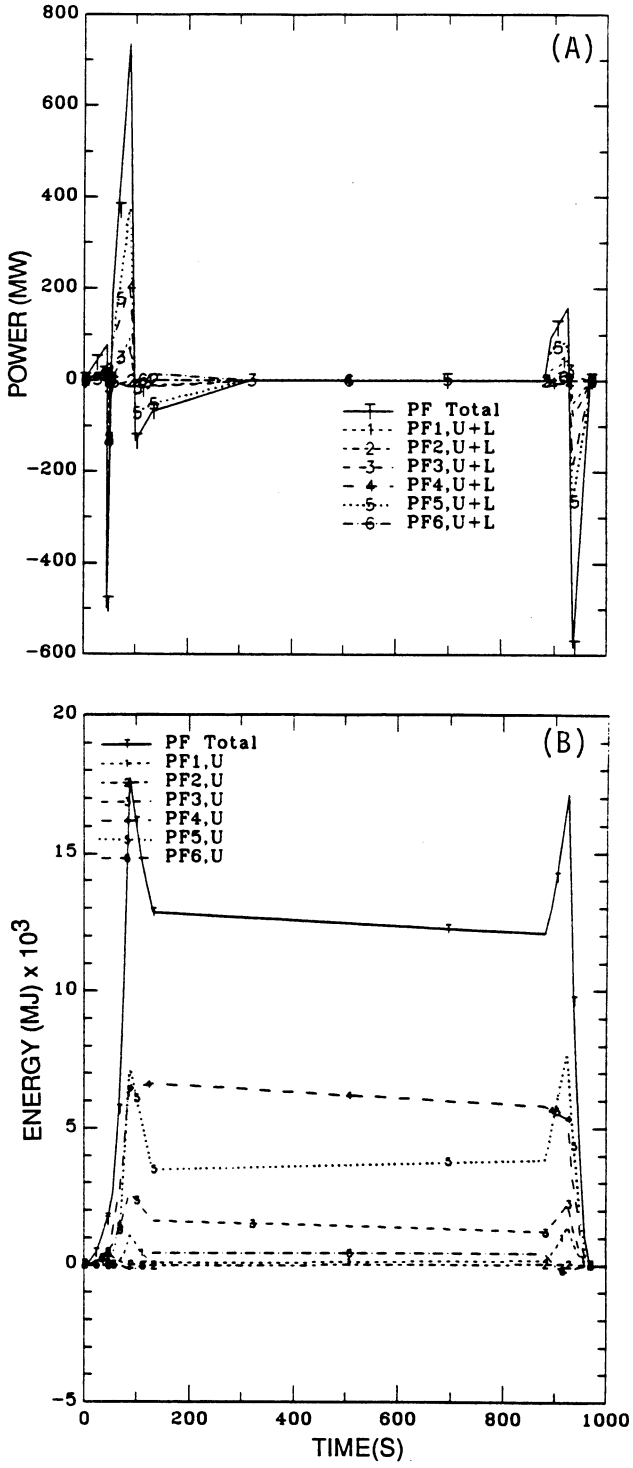

Figure 7.5-3. The possible pulsed scenario for the poloidal-field system: (A) power and (B) energy as functions of time.

plant reliability and availability. Favored circuit solutions at the 1989 workshop included the use of gate turn-off thyristors, which can operate at leading power factors, and crowbars across series supplies in order to reduce reactive power. Gate turn-off thyristors approximately double the cost and require twice the space of conventional thyristors. Crowbars require second-order additional cost and forced commutation, and they reduce the circuit slew rate for the handling of transients, such as minor disruptions. Since the workshop, the SAVAR topology invented by Boenig for the Los Alamos pulsed storage coil [29] has been suggested. This circuit uses a clever gate-firing algorithm to crowbar naturally from within the rectifier. It requires second-order additional cost, is naturally commutated, and can apply full slew rate to transients.

All PF magnets are self-supporting against tensile loads and the central solenoid is self-supporting against vertical loads. However, PF6 requires external structure at its inside radius to prevent buckling caused by compressive loads. The average hoop, axial, and Tresca membrane stresses in the conductor conduit were calculated at each point in time. The total load on each coil was also calculated following either current- or flux-conserving disruptions occurring at any time during the scenario. Even if each winding pack were entirely self-supporting, all coils would be within the static membrane allowable stress of 1000 MPa (2/3 of yield stress of a high-strength steel conduit), before and after a disruption. The highest Tresca membrane stress in a self-supporting conduit for a normal scenario is 958 MPa in PF6 at the beginning of burn, as shown in Fig. 7.5-4(A). Axial loads are not intercepted by intermediate flanges, and the vertical load from PF2 adds a worst case downward force of 170 MN on PF1 at the end of quench. There is also a 375-MN upward or separating load on PF3 that has to be supported by straps bolted to the toroidal field structure. The highest average tensile stress of 881 MPa is also in PF6, as shown in Fig. 7.5-4(B).

7.6. POLOIDAL- and TOROIDAL-FIELD PULSED LOSSES

Losses were calculated for an entire scenario in the poloidal- and toroidal-field magnet systems. Also, it was assumed that a disruption could be either current- or flux-conserving (*i.e.*, all PF coils retain their respective pre-disruption current or flux) and the effects of the two types of disruption models were calculated at any given point in the time scenario. The total losses were integrated and local heating of conductor and conduit helium was modeled in order to evaluate the energy and temperature margins of each magnet during normal scenarios and disruptions. The goal was to find a design

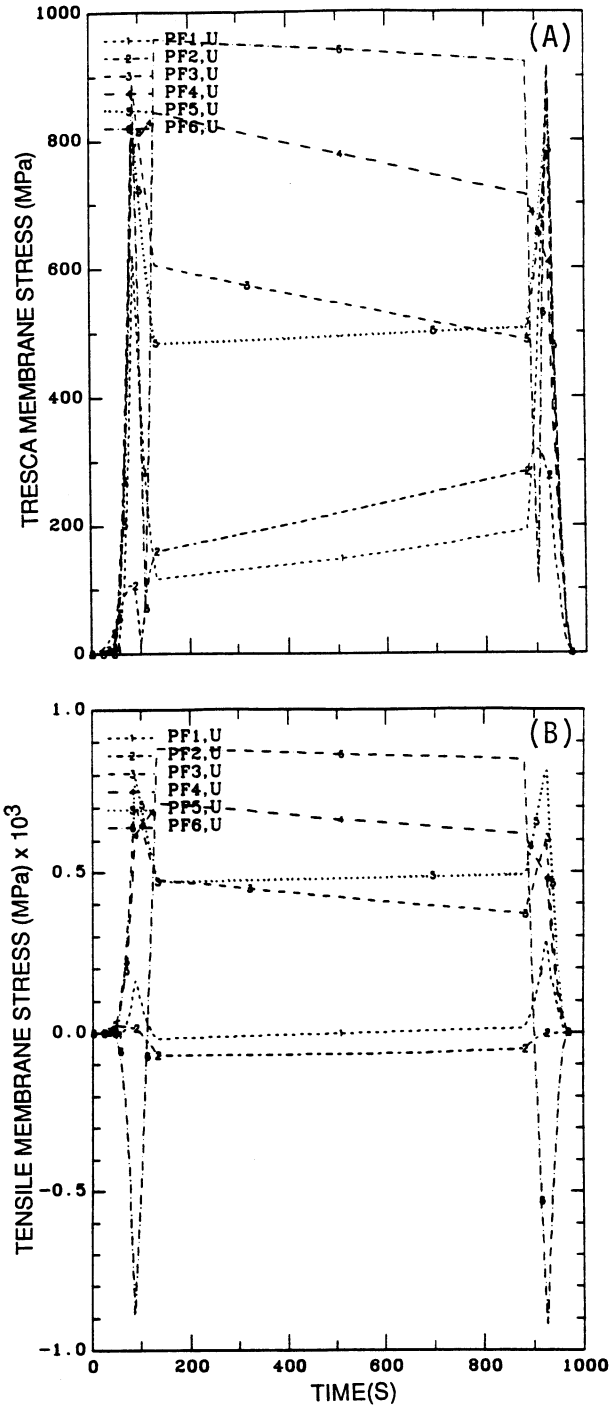

Figure 7.5-4. (A) Tresca membrane stresses (accounting for externally imposed loads) and (B) Tensile membrane stresses in conduits as functions of time for the pulsed scenario of Fig. 7.5-3.

whose margins would be everywhere greater than the above-mentioned allowables of the 0.5-K temperature margin and 0.5-J/cm^3 energy margin.

7.6.1. Method

In a typical poloidal-field scenario, currents are specified at nine points in time, each point representing the beginning or end of a scenario "event," such as start-up or burn. Linear interpolation is used between calculated points in the scenario. In the equations in Sec. 7.6.1.1, the subscripts 1 and 2 refer to the beginning and end of one interpolated time step. The loss phenomena modeled are transverse and parallel field losses due to hysteresis, coupling, and eddy currents. The coupling between diffusive mechanisms is modeled, but hysteresis and diffusion losses are modeled as though they were independent, which is a conservative assumption.

7.6.1.1. Transverse hysteresis

The form of the transverse hysteresis loss is taken from *Superconducting Magnets* [30] where Wilson's difference equation is

$$\Delta W_m = \frac{B_1^2 - B_2^2}{2\mu_o} \gamma V_{nonCu} , \tag{7.6-1}$$

where V_{nonCu} is the volume of non-copper in the conductor (m^3),

$$\gamma \equiv \frac{1}{2}\left(\frac{4}{3\beta} - \frac{0.71}{\beta^2}\right) , \tag{7.6-2}$$

$$\beta \equiv \frac{2|B_2 - B_1|}{B_{p2} + B_{p1}} , \tag{7.6-3}$$

and B_p, the transverse field for full penetration, is defined as

$$B_p = \frac{2\mu_o}{\pi} J_c D_f . \tag{7.6-4}$$

As a conservative approach to the calculation of hysteresis losses, filaments are assumed to be fully penetrated by demagnetizing fields at all times. Filament demagnetization, $M_\perp$, at a given moment in time is taken to be

$$M_\perp = \frac{2}{3\pi} J_c D_{eff} B_p (1 + \alpha^2) , \tag{7.6-5}$$

where D_f, the filament diameter in Eq. (7.6-4) is replaced with an effective diameter, D_{eff}, when experimental hysteresis loops are available. If the magnetization in an experimental hysteresis loop isn't proportional to a mandated correlation for J_c, D_{eff} can be specified as a function of field in order to match experimental data in detail. For the transverse hysteresis losses, $1 + \alpha^2$ is used as a multiplier, where α is the fraction of critical current. Then, the transverse hysteresis loss per unit length, $L_{hys,\perp}$, is

$$L_{hys,\perp} = \frac{1}{2} A_{nonCu} (M_{\perp,2} + M_{\perp,1}) |B_{\perp,2} - B_{\perp,1}| , \tag{7.6-6}$$

where A_{nonCu} is the cross-section area of the non-copper in the conductor (m^2), while $B_{\perp,1}$ and $B_{\perp,2}$ are the flux densities perpendicular to the superconducting filament, respectively, at the beginning and end of a time period.

7.6.1.2. Transverse coupling

Transverse coupling losses are calculated using Shen's method of considering a pair of twisted filaments on the edge of the matrix as the secondary of an equivalent transformer circuit [31] with a characteristic time constant of

$$\tau_\perp = \frac{\mu_o L_p^2}{4\pi^2 \rho_{eff}} , \tag{7.6-7}$$

where L_p is the twist pitch length and ρ_{eff} is the effective resistivity of the matrix. If a perfect barrier is assumed between the non-copper core and the stabilizer, ρ_{eff} is simply

$$\rho_{eff} = \rho_{nonCu} \frac{1 - \lambda}{1 + \lambda} , \tag{7.6-8}$$

where λ is the fraction of the non-copper that is actually superconductor and ρ_{nonCu} is the electrical resistivity of the non-copper (Ω-m). This fraction is impossible to actually measure but has been estimated to be 0.23 in the Large Coil Project (LCP) conductor [32]. This value (0.23) is then used for calculating losses in binary conductors. The loss has been estimated [33] to equal 0.309 in the 8717 Nb_3Sn with titanium additives used in the high-field insert of the Dual Purpose Coil (DPC) [34, 35]. Therefore, 0.309 is used as the value of λ for ternary conductors.

At the conservative extreme, if there is no barrier between the superconducting core and the surrounding copper matrix, the effective coupling resistivity of the matrix is

$$\rho_{eff,Cu} = \rho_{Cu} \frac{R_{strand}^2 + R_{nonCu}^2}{R_{strand}^2 - R_{nonCu}^2} . \tag{7.6-9}$$

R_{strand} is the outer strand radius, while R_{nonCu} is the radius of the non-copper portion of the strand. The effective resistivity for the entire conductor is then defined as:

$$\frac{1}{\rho_{eff}} = \frac{1}{\rho_{eff,Cu}} + \frac{1}{\rho_{eff,nonCu}} . \tag{7.6-10}$$

The difference equation used to calculate the local losses during a given time period is

$$\Delta W_m = \frac{1}{2\mu_o} V_{nonCu} (B_2 - B_1)^2 \frac{\tau_\perp}{\tau_\perp + (t_2 - t_1) + \tau_{passive}} , \tag{7.6-11}$$

where V_{nonCu} is the volume of an element of non-copper (superconductor plus matrix), $t_2 - t_1$ is the time period, and $\tau_{passive}$ is the characteristic time constant of the surrounding passive structure. For example, if we were considering the coupling losses within a bronze core, surrounded but isolated from stabilizer, $\tau_{passive}$ would be the sum of the time constant for eddy currents in stabilizer, conduit, and case, and passive currents in all external continuous structures.

The intrinsic resistivity of the internal Nb_3Sn matrix is believed to be the same as that of the bronze matrix. The eddy current losses in the copper stabilizer are calculated, using the same equivalent transformer approach, with a characteristic time constant of:

$$\tau_{stab} = \frac{\mu_o r_{strand}^2}{8\rho_{cu}} \left(1 + \frac{r_{bronze}^2}{r_{strand}^2}\right) \left(\frac{r_{strand}^2 - r_{bronze}^2}{r_{strand}^2}\right) V_{strand} , \tag{7.6-12}$$

where τ_{stab} is the characteristic time constant of the stabilizer, r_{bronze} is the inside radius of the stabilizer, and r_{strand} is the outside radius of the strand. If the total time constant of the LCP conductor is about 1 ms, the breakdown suggested by the equations is that about 2/3 comes from transverse coupling in the matrix and 1/3 from eddy currents in the stabilizer. This can be partially calibrated against the loss information in the Westinghouse LCP conductor reported by Wagner [36].

When experimental measurements are available, a free multiplier is used to convert L_p to $L_{p,eff}$ so that calculations will match experiments. While this technique will give correct answers, it will also conceal a broad range of assumptions about the effectiveness of the resistive barrier and, thus, should not be used to extrapolate from known to unknown conductors. However, the same technique of using $L_{p,eff}$ is utilized to match designs that assume that specified performance goals will be reached by developmental conductors.

7.6.1.3. Parallel field coupling

Parallel-field coupling losses behave as an hysteretic, not a diffusive, phenomenon because of the absence of flux cancellation by the filament or strand twist pitch. The behavior with field of these losses depends primarily on whether the field can fully penetrate a strand. The penetration field, B_p, is

$$B_p = \frac{\mu_o}{4\pi} \lambda J_\theta \,, \tag{7.6-13}$$

where λ is the non-copper fraction of the conductor metal and J_θ is the critical current density in the poloidal direction circling the filament axis. According to Miller [37], J_θ is generally less than double J_c, so that setting $J_\theta = J_c$ should give conservative results. For a conductor fully saturated by the parallel field, Miller [37] calculated the parallel coupling loss, W_m, to be

$$W_m = \frac{1}{8} \lambda J_\theta B_{||} x_o r_o \,, \tag{7.6-14}$$

where $x_0 \equiv 2\pi r_o / L_p$ is the twist pitch parameter and r_o is the equivalent radius of the composite. In the case of the LCP strands, r_o should be the radius of the central non-copper matrix and barrier in a strand.

For unsaturated conductor, the parallel coupling loss is proportional to the cube of the parallel field and is

$$W_m = W_{m,critical\ field} \frac{B_{||}^3}{B_c^3} \,. \tag{7.6-15}$$

7.6.1.4. Parallel field hysteresis

Parallel-field hysteresis losses are the parallel field losses in individual unshielded filaments. The demagnetization of a filament at full penetration by parallel field, M_c, is

$$M_c = \frac{1}{6} J_\theta D_f B_{p,c}(1 + \alpha^2) \,, \tag{7.6-16}$$

where

$$B_{p,c} = \frac{\mu_o}{\pi} J_\theta D_f \,. \tag{7.6-17}$$

Individual filaments are assumed to be fully saturated by the parallel field, so the parallel demagnetization of the filaments, $M_{||}$, is

$$M_{||} = M_c \frac{B_{||}}{B_c} \,. \tag{7.6-18}$$

This is clearly a conservative assumption, since parallel coupling has not been assumed to have saturated fields and may provide substantial shielding of individual filaments.

The loss per unit length due to parallel hysteresis losses, $L_{hys,||}$, has the same form as that for transverse hysteresis [Eq. (7.6-6)] and is

$$L_{hys,||} = \frac{1}{2} A_{nonCu} \left(M_{||,2} + M_{||,1}\right) \left|B_{||,2} - B_{||,1}\right| . \tag{7.6-19}$$

7.6.2. Case and Conduit Pulsed Losses

The transverse-field eddy-current losses in a hollow rectangular case are also calculated using the transformer secondary method. The characteristic time constant of the case to transverse fields, $\tau_{\perp}$, is given by

$$\tau_{\perp} = \frac{\mu_o W_{case} t_{eq,case}}{4 \rho_{case}} , \tag{7.6-20}$$

where W_{case} and $t_{eq,case}$ are, respectively, the width and the thickness of the conduit or case. The characteristic time constant of the case for parallel fields, $\tau_{||}$, is half that for transverse fields, *i.e.*,

$$\tau_{||} = \frac{\mu_o W_{case} t_{eq,case}}{8 \rho_{case}} . \tag{7.6-21}$$

If the case or conduit is not square and/or the walls are of different thicknesses, time constants are approximated by calculating the resistance and inductance separately. The resistance is clearly the sum of the resistance of each of the four walls. For a thin walled case, the inductance per unit length is just the width or height of the wall transverse to the flux change being calculated. Alternatively, the approximation recommended by the NET team [38] is

$$P_{eddy,\perp} = \frac{1}{15} \frac{(dB/dt)^2}{\rho} \frac{w_o^3 h_o^3}{w_o^2 + h_o^2} , \tag{7.6-22}$$

where $P_{eddy,\perp}$ is the loss per unit length, while w_o and h_o are, respectively, the outside width and height of the conduit or case. For parallel fields

$$P_{eddy,||} = \frac{1}{15} \frac{(dB/dt)^2}{\rho} \left(\frac{w_o^3 h_o^3}{w_o^2 + h_o^2} - \frac{w_i^3 h_i^3}{w_i^2 + h_i^2} \right) . \tag{7.6-23}$$

7.6.3. Results

The losses in both the poloidal- and toroidal-field systems are dominated by hysteretic mechanisms. If this were not the case, the scenario could be slowed down to put more of a burden on RF assistance. Since the burn is steady state, the PF magnets are only required to absorb pulsed field energy during startup, shutdown, and off-normal conditions such as plasma disruptions. Unlike ITER, there is no problem of temperature ratcheting between pulses. Figure 7.6-1(A) shows a pseudo-scenario used to represent the characteristics of the poloidal-field system during startup and shutdown, and during changes in beta and flux linkage during the burn. The duration of the burn is substantially longer than is shown, but the losses calculated in this section are insensitive to the value of flattop since they are determined by hysteretic losses. The short duration of the flattop is a convenience for displaying the results.

The total pulsed-energy loss in the poloidal-field system during a full scenario (startup, burn, and shutdown) is 1.6 MJ, as shown in Fig. 7.6-1(A), while that in the toroidal-field system is 1.06 MJ, as shown in Fig. 7.6-1(B). This energy can be absorbed adiabatically and is easily removed during the long pulse or shutdown periods. Figure 7.6-1(B) shows that the peak energy per pulse absorbed in the toroidal-field winding increases to 1.99 MJ following a current-conserving disruption at the end of plasma quench.

In order to interpret the results for the disruption case, it should be understood that during the pseudo-scenario, the energy absorbed by the coils is determined by the difference between the disruption case and the normal case. In this way, the results from a disruption at any time during the pulse (*i.e.*, during startup, shutdown, high or low beta, and with different flux linkage during the burn) can be easily determined.

The effects of disruptions on the PF coils are shown in Fig. 7.6-2. The hysteresis losses in the poloidal-field system during ramp-down are larger than disruption losses, so that neither current- nor flux-conserving disruptions can increase the pulsed losses in the system. The improved pulsed-energy-loss performance should also increase the feasibility of collector sweeping, which was previously evaluated as impractical with a tape winding in the TF magnet.

The worst-case energy margin in the poloidal-field system is in PF3, which is the only PF coil that was space constrained after the last magnetohydrodynamic (MHD) iteration. The minimum energy margin is 0.62 J/cm^3 at the end of start-up for a normal scenario, as shown in Fig. 7.6-3. The temperature margin is 1.5 K at that time, as shown in Fig. 7.6-4 where the current-sharing temperature and the bath temperature are

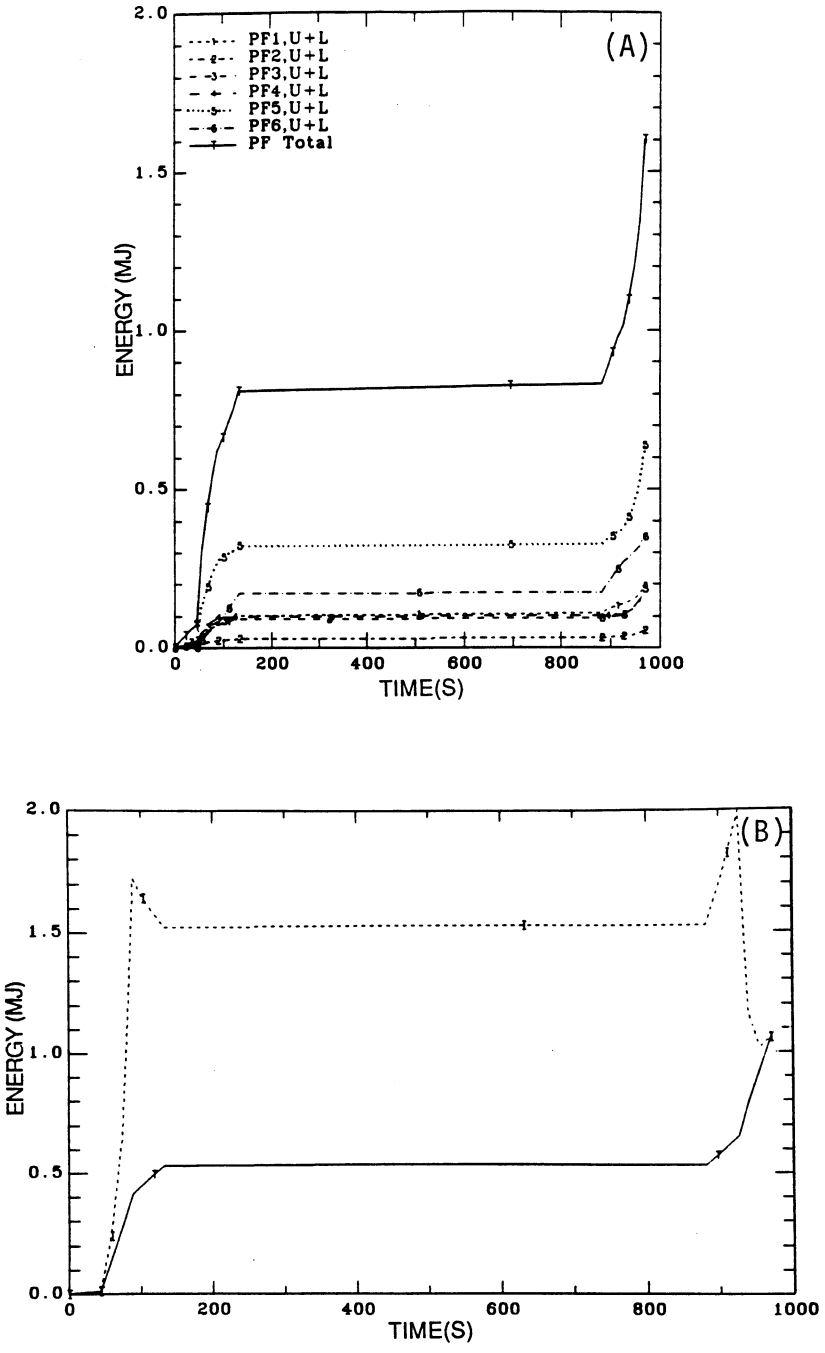

Figure 7.6-1. Pulsed-energy losses as functions of time in (A) individual PF windings (normal scenario) and (B) TF windings (normal scenario plus current-conserving disruption).

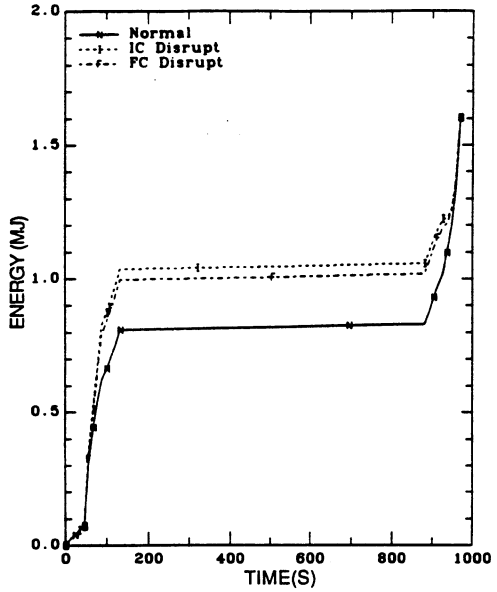

Figure 7.6-2. Total losses in PF windings as a function of time (current- or flux-conserving disruption).

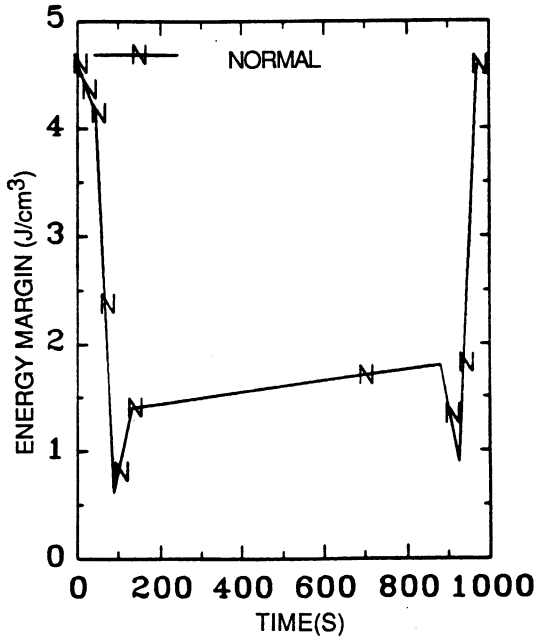

Figure 7.6-3. Minimum energy margin in PF3 (normal operation) which is the worst case in the poloidal-field system.

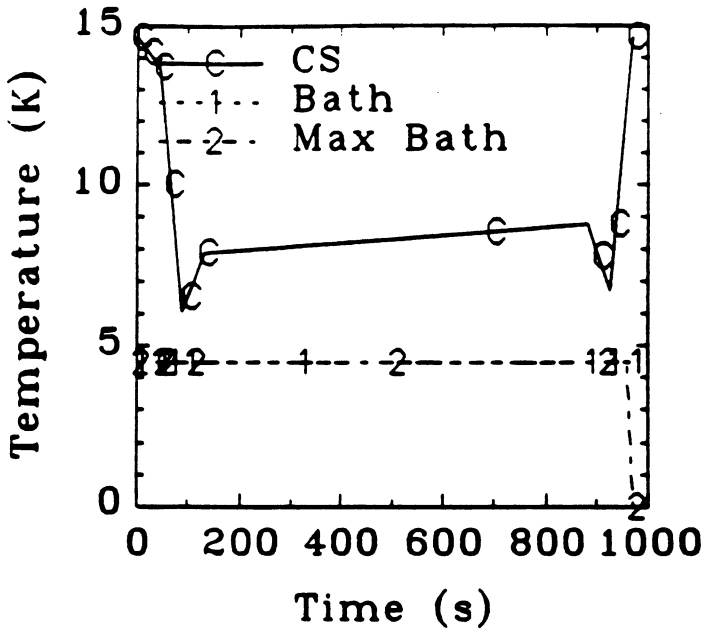

Figure 7.6-4. Current-sharing temperature and bath temperature at worst location of ARIES-I PF coil (normal operation).

shown. As a conclusion, the poloidal-field system is very robust, and the pulsed losses are manageable.

Next we consider the pulsed losses in the toroidal-field system. The energy margin in the TF magnet is necessarily lower than the PF magnet because of the high field and lower helium fraction, as shown in Fig. 7.6-5. In order to have an adequate energy margin against disruptions, the fraction of the conductor envelope of the helium in the high-field grade was increased from 1.4% to 7% by reducing the cross section of the structure in the first grade. Also, while the bulk of the magnet has a bath temperature of 4.2 K, the inlet helium temperature of the first row had to be subcooled to 3.8 K. The lowest energy margin is 140 mJ/cm^3. Although sufficient for stability, the calculated energy margin is less than the conservative desired allowable for ITER of 500 mJ/cm^3. The highest heat deposition at the worst location from a current-conserving disruption is 30 mJ/cm^3, as seen in Fig. 7.6-6. However, this deposition occurs at a point with relatively large energy margin and is less limiting that the 30 mJ/cm^3 shown in Fig. 7.6-5.

The heat flux for transition to the ill-cooled regime is 3.3 W/cm^2 at the worst location on the high-field side, which is at a height of 1.88 m above the equator. The Joule heat

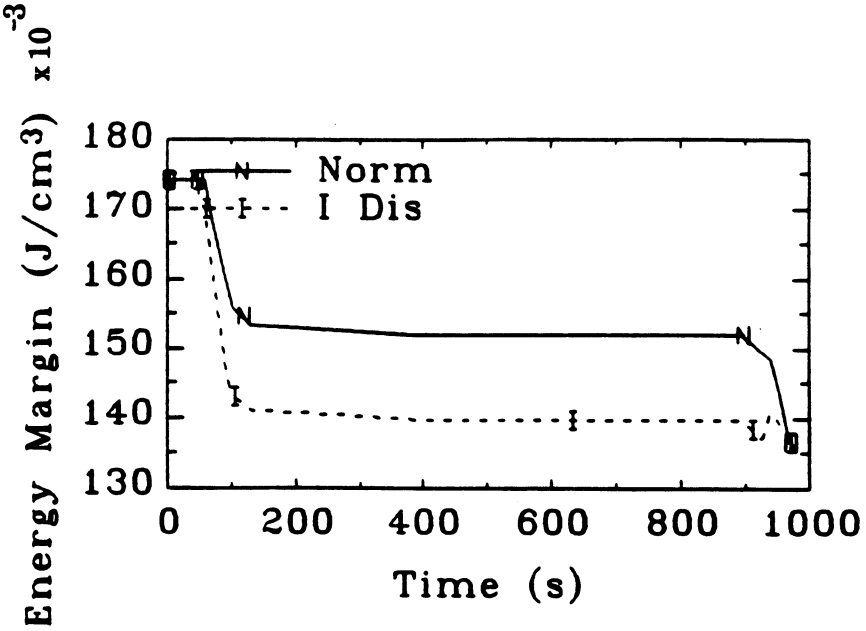

Figure 7.6-5. Worst-case energy margin of TF coil (normal operation and disruption).

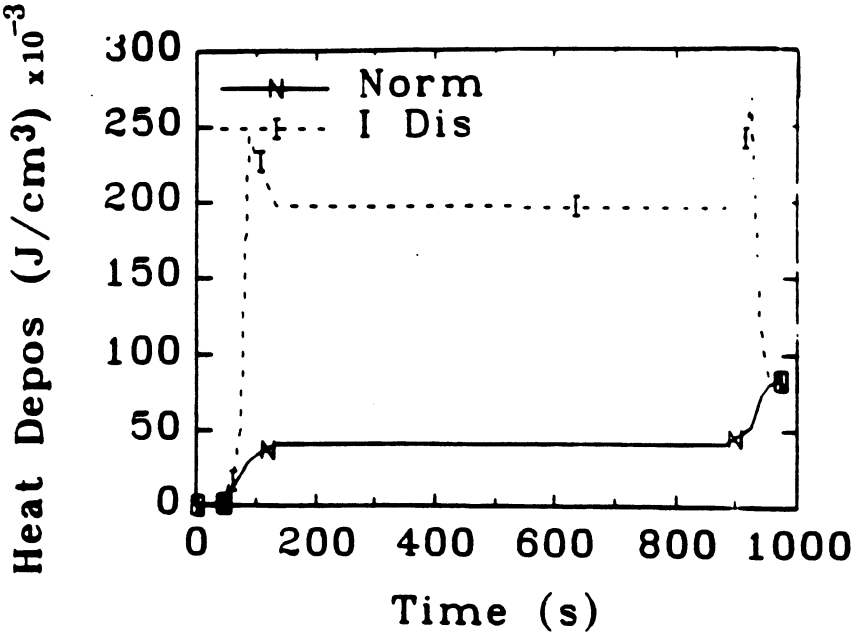

Figure 7.6-6. Maximum heat deposition in coil (normal operation and disruption). The maximum heat deposition, however, occurs at a point with relatively large energy margin.

flux is shown in Fig. 7.6-7. Since the Joule heat flux is only 0.911 W/cm^2, the cable conductor will be in the well-cooled regime. Finally, Fig. 7.6-8 shows the highest bath temperature in the first turn for normal operation.

7.7. COSTING

In this section, the costing models of the TF and PF coils are described. Since the TF coils are beyond the state of the art, while the PF coils are no more demanding than the ITER poloidal-field system, different costing algorithms were used. They are described separately below.

7.7.1. Toroidal-Field Costing

A simple procedure for costing the TF coils is proposed. This procedure combines the algorithms described by Thomson [39] for calculating the costs of the individual components of the TF coil with simple algorithms for determining the weights of the components.

It is assumed that the conductor (Nb_3Sn) costs are similar to those of internally cooled, cabled superconductors (ICCS) today. Although more advanced, the general characteristics of the fabrication are comparable and the materials are very similar to available conductors.

The stabilizer is more sophisticated than is used in today's conductors and we have allowed for a doubling of the cost of the base material to about \$30/kg. Similarly, the cost of the structural material (as sheets of 316 SS or Incoloy) has been assessed to about \$25/kg (cost of high-quality thin sheets of Incoloy at today's prices). Furthermore, \$10/kg has been allocated for increased cost of manufacturing. The bulk of the structural material of the TF coil is basically plates. The relatively complex plates could be manufactured by putting several thinner plates of different sizes and thicknesses together. Therefore, complex machining and cutting/welding is kept to a minimum. It is possible today to manufacture the Incoloy plates to thickness and sizes relevant for ARIES-I. The finished cost of the structural plates is \$75/kg (*versus* \$50/kg for the typical costs of commercial complex structures, tenth-of-a-kind, utilized by Thomson [39]).

The total cross-sectional area of the magnet is determined from

$$A_{tot} = A_{sc} + A_{stab} + A_{str} + A_{He} + A_{ins} , \qquad (7.7\text{-}1)$$

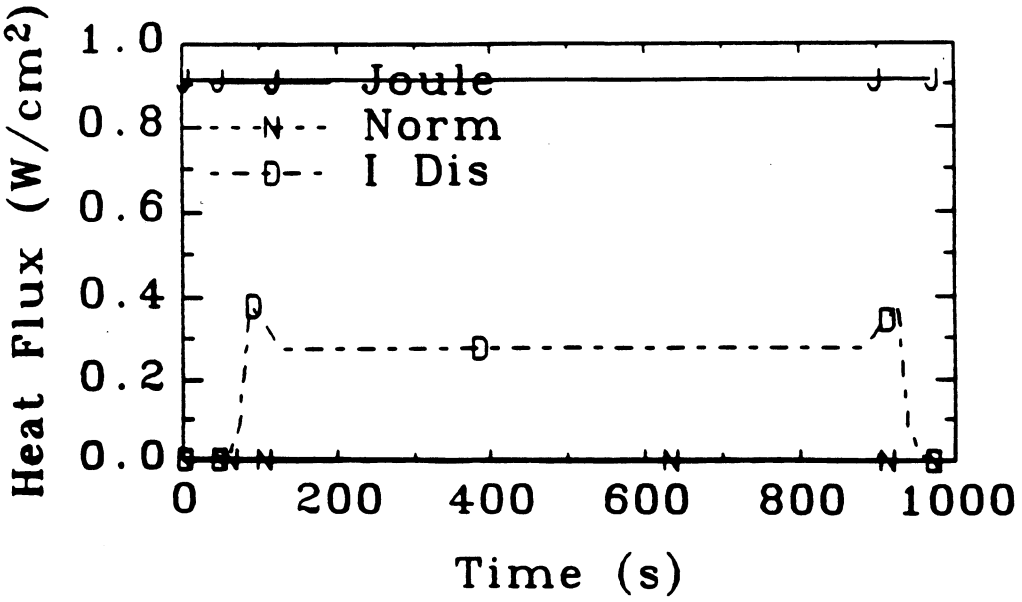

Figure 7.6-7. The Joule heat flux (normal operation and disruption).

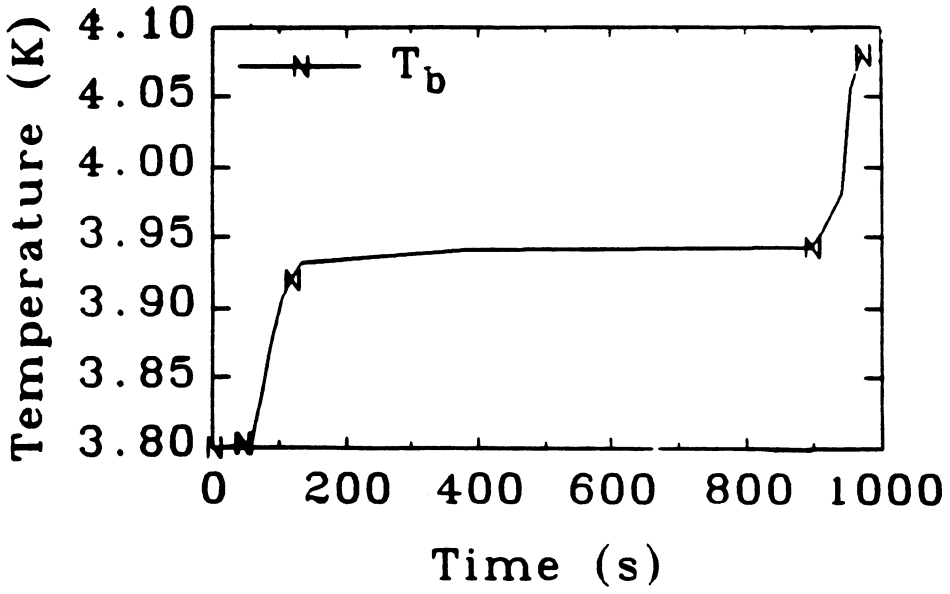

Figure 7.6-8. Maximum bath temperature of first turn of TF coil (normal operation).

where A_{sc}, A_{stab}, A_{str}, A_{He}, and A_{ins} are, respectively, the areas of the superconductor, the copper stabilizer, the structure, the He cooling fraction, and the insulation. The cross-sectional areas are determined by the methods described in Sec. 7.4. The length of the conductor per turn is easily determined and will be denoted by ℓ. Then, the total volume of each of the elements is determined by $A \times \ell \times n_{coils}$. This can be repeated for all of the components of the TF coil.

The amount of structure in the conductor, as opposed to the case, is all that remains to be calculated. We are assuming the use of plates in which the superconductor is embedded (as in the HFCTR design concept [1] and the Westinghouse LCP coil [32]). These plates support the radial loads and help support the vertical loads. They are made of high-strength structural material (either metal or composite, still to be determined). The conductor is an ICCS conductor; we assume that 15% of the cross-sectional area of the copper and superconductor is the conduit. Therefore, the structural material in the cables is $0.15 \times (A_{sc} + A_{stab})$. The rest of the structural material is in the plates and should be costed at the same rate as the toroidal-field case material ($75/kg).

Detailed modeling of the TF magnet results in the component fractions shown in Table 7.7-I. The fraction of the winding pack is f_{pack}, and the fraction of the overall magnet is f_{magnet}. The costing is shown in Table 7.7-II. The unit cost of this type of magnet is about $95/kg.

7.7.2. Poloidal-Field Costing

The poloidal-field costs were determined according to the cost algorithm proposed by Miller and adopted by the ITER magnet unit for superconducting magnet costing [28]. These algorithms are sufficiently detailed and realistic to correctly take into account the amount of superconductor, stabilizer, structure, and insulation, and the complexity of winding and assembly. The cost equations used are:

$$\begin{aligned}
\text{Cost}_{wire} &= (650 - 600 f_{Cu})\ (\$/\text{kg})\,, \\
\text{Cost}_{cabling} &= 20\ (\$/\text{m})\,, \\
\text{Cost}_{sheathing} &= 60\ (\$/\text{m}) + 30\ (\$/\text{kg})\,, \\
\text{Cost}_{insertion} &= 2\ (\$/\text{m})\,, \\
\text{Cost}_{winding} &= 125\ (\$/\text{kg})\ \text{of winding}\,, \\
\text{Cost}_{case} &= 75\ (\$/\text{kg})\ \text{of case}\,, \\
\text{Cost}_{closeout} &= 5\ (\$/\text{kg})\ \text{of total mass}\,.
\end{aligned} \tag{7.7-2}$$

Table 7.7-I.
Component Fractions for ARIES-I TF Coils

	f_{pack}	f_{magnet}
Plates	0.573	0.450
Conduit	0.045	0.028
Stabilizer	0.241	0.186
Superconductor	0.057	0.044
Case	–	0.226
Insulator	0.046	0.036
Helium	0.043	0.033

Table 7.7-II.
ARIES-I TF-Coil Costing Calculations

	f_{magnet}	Unit Cost (\$/kg)	$f_{magnet}\times$ Unit Cost
Conduit	0.028	50	1.4
Stabilizer	0.186	70	13.0
Superconductor	0.044	400	17.6
Total winding	0.258	50	12.9
Plates	0.450	75	33.7
Case	0.226	75	17.0
Insulator	0.036		
Helium	0.033		
Averaged unit cost of the TF coil (\$/kg)			95

Table 7.7-III.
Cost of the ARIES-I PF Coils[a] (k$)

Coils	Wire	Cabling	Sheath	Insertion	Winding	Case	Closeout	Total
PF1	1,988	138	1,312	13	4,874	108	202	8,637
PF2	2,173	104	885	10	4,629	108	192	8,102
PF3	10,499	138	1,643	13	12,875	96	521	25,788
PF4	7,000	314	2,395	31	11,766	210	484	22,203
PF5	5,227	589	4,196	58	12,727	411	536	23,746
PF6	424	196	884	19	1,418	274	75	3,291
Total	27,312	1,480	11,213	148	48,290	1,210	2,012	91,666

[a]Including both upper and lower coils.

These equations are intended for ITER, a first-of-a-kind experimental reactor. Since ARIES-I is a tenth-of-a-kind reactor, the cost in current dollars is reduced by $10^{0.2}$. The detailed costs of the ARIES-I PF coils are shown in Table 7.7-III.

7.8. SUMMARY AND CONCLUSIONS

The critical issues of the toroidal- and the poloidal-field systems for the ARIES-I design have been presented in this section. The design of the TF magnet is driven by the high field (21 T) and by the decision to limit the use of advanced magnet materials (both for the conductor and the structure) to those that already exist in the laboratory (although extrapolations to the sizes and lengths required for use in a tokamak fusion-power reactor may be required). The reference design for the TF magnet uses plates of 316 SS or Incoloy 908 and internally cooled, cabled, Nb_3Sn-ternary superconductor. The stabilizer is CuNb which carries structural loads.

The successful operation of a superconducting toroidal-field system with $B > 20$ T and $E_{stored} > 100$ GJ will require a significant development program. Presently, many of

the materials used in this design are only available in small laboratory samples and are not optimized for the desired properties (*e.g.*, strength, current density, *etc.*).

At present (1990), the record for highest field produced by a superconducting magnet is held by P. Turowski and T. Schneider [40]. They built and tested a superconducting magnet (using only superconductors) that operates at 20.1 T. It is a hybrid system (equivalent to our grading of the magnet conductor), with a NbTi outer magnet and several Nb_3Sn inserts. The magnet is cooled at 1.8 K.

A magnet-technology development program leading to the availability of the 21-T ARIES-I TF-magnet system in 20 to 25 years is outlined in Fig. 7.8-1. The development of superconducting materials, structural materials, and magnets is illustrated. Each magnet is based upon success in the materials development programs.

The design of the PF-magnet system does not share the feasibility and development issues of the toroidal-field system. The PF coils in ARIES-I are external to the toroidal-field system. They are superconducting, using internally cooled, cable-in-conduit conductor. The peak field in the poloidal-field system is only 12.8 T. Normal and off-normal pulse losses in the PF- and TF-coil systems are sufficiently low so that they do not impact overall refrigeration requirements. The magnets have built-in margins that are sufficient to survive disruptions without quenching.

		1990	1995	2000	2005	2010	2015	2020
STRUCTURAL MATERIALS	INCOLOY Fe-Cr-Ni	Alloying	Mechanical Testing	Irradiation Testing				
					Fiber/Matrix Compatibility in Environment	Complete Mechanical Database	Large scale Manufacturing	
	Fibers	Property Optimization		Small scale				
		Coating Development		Composites				
SUPERCONDUCTORS	Nb_3Sn	Long lengths via P/M	Complete Property Database	Conductor Development and Testing	High Field Magnet Applications	Large-Scale Manufacturing		
						Testing: stability, mechanical		
	Nb_3 (Al,Ge) NbN	Process Optimization	Long lengths Wider Tapes	Complete Property Database	Conductor Development and Testing		irradiation, strain bending	
MAGNETS	Large Solenoids		20 T		22 T		24 T	
	TF COILS	13 T				20 T		24 T

Figure 7.8-1. Magnet-technology development path.

REFERENCES

[1] J. H. Schultz, F. S. Malick, D. R. Cohn, and J. E. C. Williams, "High Field Compact Tokamak Reactor," in *Proc. IEEE 8th Symp. Eng. Prob. Fusion Res.* (Oct. 1979) IEEE, Piscataway, NJ (1980).

[2] L. Bromberg and D.R. Cohn, "High Field Tokamak Reactors," *Proc. 4th Tech. Comm. Mtg. and Wkshp.*, Yalta, USSR (1986), *Fusion Reactor Design and Technology 1986*, IAEA-TC 392.3, IAEA, Vienna (1987) p. 211.

[3] D. R. Cohn and L. Bromberg, "Advantages of High Field Tokamaks for Fusion Reactor Development," *J. Fusion Energy* **5** (1986) 161.

[4] S. Foner, C. L. H. Thieme, S. Pourrahimi, and B. B. Schwartz, "Practical Processing of A-15 Multifilamentary Superconducting Wire from Powders: $Nb_3A\ell$ and Nb_3Sn," *Adv. Cryo. Eng.* **32** (1986) 1031.

[5] S. Pourrahimi, C. L .H. Thieme, and S. Foner, "21 Tesla Powder Metallurgy Processed Nb_3Sn(Ti) Using (Nb-1.2 wt %Ti) Powders," *IEEE Tran. Magn.* **Mag-23** (1987) 661.

[6] K. Togano, H. Kumakura, and K. Tachikawa, "Preparation of High Field $Nb_3A\ell$ and $Nb_3(A\ell,Ge)$ Superconducting Tapes by an Electron Beam Annealing," *IEEE Tran. Magn.* **MAG-23** (1987) 960.

[7] H. Kumakura, K. Togano, K. Tachikawa, Y. Yamada, S. Murase, E. Nakamura, and M. Sasaki, "Synthesis of Nb_3Ga and $Nb_3A\ell$ Superconducting Composites by Laser Beam Irradiation," in *App. Phys. Lett.* **48** (1986).

[8] K. Togano and K. Tachikawa, "Fabrication of $Nb_3A\ell$ Based Superconductors by Continuous Quenching Techniques," in *Adv. Cryo. Eng.* **34** (1988).

[9] H. Kumakura, K. Togano, T. Takeuchi, and K. Tachikawa, "Studies on Structure and Properties of *In-Situ* V_3Ga Superconducting Composite Tapes," *IEEE Tran. Magn.* **MAG-21** (1985) 760.

[10] K. Oishi, N. Takei, Y. Tanaka, and K. Yamada, "Development of High Field Superconducting Magnet by Using *In-Situ* V_3Ga Compound Tape," in *Proc. Magnet Technol.* **10** (1987).

[11] K. Suemune, T. Sakamoto, T. Ogawa, T. Okazaki, and S. Maehara, "Manufacture and Properties of Nitrogen-Containing Cr-Mn and Cr-Ni Austenitic Stainless Steels for Cryogenic Use," *Adv. Cryo. Eng.* **34** (1988) 123.

[12] H. Nakajima, K. Yoshida, M. Oshikiri, Y. Takahashi, K. Koizuma, S. Shimamoto, M. Shimada, S. Tone, S. Sakamoto, K. Suemune, and K. Nohara, "Tensile Properties of New Cryogenic Steels as Conduit Materials of Forced Flow Superconductors at 4 K," *Adv. Cryo. Eng.* **34** (1988) 173.

[13] J. Martin, R. G. Ballinger, M. M. Morra, M. O. Hoenig, and M. M. Steeves, "Tensile, Fatigue, and Fracture Toughness Properties of a New Low Coefficient of Expansion Cryogenic Structural Alloy, Incoloy 9XA," in *Adv. Cryo. Eng.* **34** (1988).

[14] M. M. Morra, I. S. Hwang, R. G. Ballinger, M. M. Steeves, and M. O. Hoenig, "Effect of Cold Work and Heat Treatment on the 4-K Tensile, Fatigue and Fracture Toughness Properties," in *Proc. Magnet Technol.* **11** (1989).

[15] R. G. Ballinger, Massachusetts Institute of Technology, private communication (1988)

[16] T. Hamada, T. Nishida, Y. Sajiki, M. Matsumoto, and M. Endo, "Structures and Physical Properties of Carbon Fibers from Coal Tar Mesophase Pitch," *J. Mater. Res.* **2** (1987) 850.

[17] "Torayca Technical Reference Manual," in *Information on Available Materials from Toray Industries, Inc.*, brochure from Toray Industries, Inc. (1988).

[18] "Ultra High Modulus Carbon Fiber," in *Du Pont Fiber G, Technical Specifications for E-130*, brochure from Du Pont (1989).

[19] N.S. Wheeler and D.S. Lashmore, "Electroforming Metal Matrix Composite Precursors," American Cyanamid and Institute for Materials Science and Engineering, National Bureau of Standards annual report NBS-AR-1989 (1989).

[20] O. Hoffman, "The Brittle Strength of Orthropic Materials," *J. Composite Mater.* **1** (1967) 200.

[21] C. C. Chamis, "Failure Criteria for Filamentary Composites," NASA Lewis Research Center report NASA TN D-5367 (1969).

[22] C. C. Chamis, "Design Analysis and Structural Synthesis of Multilayered Filamentary Composites," Ph.D. thesis, Case Western Reserve University (1967).

[23] H. R. Hart, Jr., "Magnetic Instabilities and Solenoid Performance: Applications of the Critical State Model," in *Proc. 1968 Summer Study on Superconducting Devices and Accelerators, Part II.*, Brookhaven National Laboratory report BNL 50155 (C-55) (1968).

[24] C. P. Bean, "Magnetization of Hard Superconductors," *Phys. Rev. Lett.* **8** (1962) 562.

[25] S. Shimamoto, H. Nakajima, K. Yoshida, and E. Tada, "Requirements for Structural Alloys for Superconducting Magnet Cases," *Adv. Cryo. Eng.* **32** (1988) 23.

[26] "ITER Conceptual Design Report," ITER Documentation Series No. 3, International Atomic Energy Agency, Vienna (1989).

[27] M. Suenaga, unpublished data presented at DOE Workshop on Conductor-Sheath Issues for ICSS, Boulder, CO (July 1985).

[28] J. Miller *et al.*, "Report of Work by the Magnet Design Unit," International Atomic Energy Agency report ITER-EL-MG-1-9-3 (1989); also Lawrence Livermore National Laboratory report LLNL-ITER-89-048 (1989).

[29] H. Boenig and F. Cibulka, "A Static VAR Compensator Using a Superconducting Coil" *IEEE Trans. Power Apparatus & Systems* **10** (1982) 259.

[30] M. N. Wilson, *Superconducting Magnets,* Clarendon Press, Oxford (1983).

[31] S. S. Shen and R. E. Schwall, "Transient Loss Analysis and Measurements on Normal Conductors and Composite Superconductors," in *Proc. Int. Cryo. Eng. Conf.*, Boulder, CO (July 1978).

[32] "IAEA Large Coil Task; Chapter 3: Characteristics of the Coils," D. S. Beard, W. Klose, S. Shimamoto, and G. Vecsey, Eds., *Fusion Eng. Des.* **7** (1988) 23.

[33] D. Smathers, Teledyne Wah-Chang, private communication (1989).

[34] M. M. Steeves, T. A. Painter, M. Takayasu, R. N. Randall, J. E. Tracey, I. S. Hwang, and M. O. Hoenig, "The U.S. Demonstration Poloidal Coil," *IEEE Trans. Magn.* **Mag-27** (1991) 2369.

[35] T. Ichihara *et al.*, "Fabrication of the Demo Poloidal Coils," *IEEE Trans. Magn.* **MT-11** (1989) 1342.

[36] G.R. Wagner, "Transverse Field AC Losses in the Westinghouse Nb_3Sn Force-Cooled LCP Conductor," *Proc. IEEE 8th Symp. Eng. Prob. Fusion Res.* (Oct. 1979) IEEE, Piscataway, NJ (1980) 834.

[37] J. R. Miller and S. Shen, "Experimental Simulation of Pulsed Field Losses in Tokamak Toroidal Field Coils," *IEEE Tran. Magn.* **Mag-13** (1977) 623.

[38] C. Kwasnitza, "Basic Equations for the Calculation Of AC Losses in the Conductor for the Superconducting NET TF Coils," KfK Karlsruhe report KRYO-86-13 (1986).

[39] S. L. Thomson, "Cost Algorithms for Superconducting Magnets," Oak Ridge National Laboratory report FEDC-M-88-ITER-001 (1988).

[40] P. Turowski and T. Schneider, "A 20-T Superconducting Magnet System," *Physica B* **155** (1989) 97.